Engineering Fracture Mechanics 325 (2025) 111291

Contents lists available at ScienceDirect

Engineering Fracture Mechanics

journal homepage: www.elsevier.com/locate/engfracmech

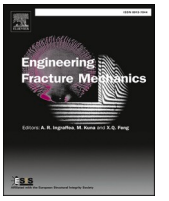

# A novel multiscale crack propagation modeling approach based on adaptive coupling of peridynamics and boundary element method

Yang Yang [a,*], Xun Wei [a], Yijun Liu [b]

[a] Faculty of Material Science, Shenzhen MSU-BIT University, Guangdong, China
[b] Department of Mechanics and Aerospace Engineering, Southern University of Science and Technology, Guangdong, China

ARTICLE INFO

*Keywords:*
Multiscale crack propagation
Peridynamics
BEM
Adaptive coupling
Macro crack
Micro crack

ABSTRACT

This paper introduces an innovative multiscale method for predicting crack propagation by integrating the peridynamics (PD) with the boundary element method (BEM) in an adaptive framework. This proposed algorithm autonomously predicts the path and direction of crack propagation without requiring predefined crack trajectory domains. Microcrack propagation is accurately tracked using bond-based PD approach, which specifically focuses on the crack tip field. The overall response of the structure and the behavior of macrocracks are simulated using the dual BEM. The evolution of the cracks is automatically captured through the adaptive coupling of these two algorithms via iterative of displacements continuity and force equilibrium. Throughout the analysis, the geometry and discretization of the PD domain remain unchanged, which helps limit the non-local computational domain and significantly reduces the computation time. Macrocracks are treated as boundaries of the entire structure, simplifying the implementation process. The accuracy of this method is verified through analytical results using various PD domains. Additionally, its efficiency is demonstrated through several examples of crack propagation predictions. The results demonstrate that this algorithm has the potential for applications in the crack propagation analysis of actual structural components.

## 1. Introduction

Multi-scale crack propagation refers to the continuous expansion process of cracks from the microscale to the macroscale. Understanding this phenomenon is critical in the fields of material science and engineering, as it influences the integrity and durability of structures. Among various methods for analyzing crack propagation, the peridynamic (PD) approach [1] has gained recognition for its ability to capture the intricate behaviors of cracks at both micro- and nano-scales. The primary advantage of PD lies in its capacity to account for non-local interactions, which allows for a more accurate representation of stress fields around the crack tips. PD can spontaneously capture all failure modes, including crack nucleation, propagation, and branching. This capability is particularly beneficial when dealing with heterogeneous materials, where the influence of microstructural features on crack behavior is significant.

PD has been applied in modeling the propagation of cracks in various types of materials and under different loadings. For example, Karpenko et al. [2] examined how various types of small defects affect crack propagation in brittle materials. Chen et al. [3,4] focused on the crack propagation and fatigue crack growth in hydrogels. Wang et al. [5] created a mesoscale model to study the impact of micro-void defects on the transverse mechanical properties of composites. Ozdemir et al. [6] performed a detailed investigation of the

* Corresponding author.
*E-mail address:* yangy2023@smbu.edu.cn (Y. Yang).

https://doi.org/10.1016/j.engfracmech.2025.111291
Received 7 March 2025; Received in revised form 23 April 2025; Accepted 27 May 2025
Available online 6 June 2025

interactions between macrocracks and microcracks in functionally graded materials. Hu et al. [7] introduced a PD model for composite laminates that accounts for transverse shear deformation and material coupling. Shen et al. [8] modeled beams and shells with PD using an interpolation method while also considering the effects of transverse shear. Yang et al. [9–11] presented PD formulations for Mindlin plates, higher-order beams, and higher-order plates. Zhang et al. [12] derived the PD Reissner–Mindlin shell theory. Yang et al. [13] conducted a fracture analysis of hyperelastic membranes. Zhang et al. [14] proposed a stabilized peridynamic correspondence material model for axisymmetric problems to effectively simulate the ablation and ductile facture behaviors of metals under high temperatures. Li et al. [15] presented an implicit stabilized non-ordinary state-based peridynamic method to simulate the finite deformation and crack propagation in nearly incompressible hyperelastic materials.

Despite its advantages in simulating crack propagation and other aspects, PD faces challenges related to computational efficiency. The non-local nature of the interactions necessitates the consideration of a larger domain, which results in increased computational costs and time. This limitation has prompted researchers to explore hybrid approaches to improve the computational efficiency of PD [16,17], such as using parallel computing [18,19] and machine learning techniques for acceleration [20,21]. These methods can help reduce the computational cost of PD to some extent, but they are still impractical for analyzing the response and crack propagation in large structures, particularly in modeling the evolution of multiscale cracks.

The integration of PD with continuum mechanics approaches can enhance computational efficiency while maintaining accuracy in crack propagation analysis. In recent literature, there have been various methods for coupling continuum mechanics approaches with PD. One prominent approach is the domain decomposition strategy [22–25], where the continuum mechanics model is applied to the far-field regions while PD is used in the near-field zone surrounding the crack. This method typically involves the following steps: (1) defining the problem domain and identifying the crack location, (2) applying continuum mechanics to model the stress and displacement fields in the far-field, (3) employing PD to analyze the behavior in near-field, and (4) ensuring compatibility and equilibrium between the two regions. While this method enhances computational efficiency, it may suffer from issues related to the continuity of the stress field at the interface of the two models. It is crucial to recognize the damaged region before making modeling arrangements. Another approach is the use of a multi-scale method that integrates PD with finite element methods (FEM) [26,27]. This technique proceeds as follows: (1) conducting a coarse-scale analysis using FEM to capture the overall structural response, (2) refining the model in areas where crack propagation is anticipated, and (3) applying PD to these refined regions to accurately simulate crack behavior. Although this method balances accuracy and computational cost, challenges remain in ensuring seamless integration between the different scales. A broad area should be designated for PD where crack propagation may occur. If possibilities of multiple crack growth are present, this can lead to increased computational costs and reduced efficiency in the coupling method. Recently, a few adaptive coupling works between PD and FEM have been introduced [28–30]. Alebrahim et al. [31] proposed another adaptive PD-FEM model to investigate static crack propagation in brittle and quasi-brittle materials. This adaptive method employs various operations, such as interpolation, refinement, remeshing and switching, to implement the PD solution in the FEM domain wherever necessary. However, the entire structure domain should be modeled with PD, and switching from FEM nodes to PD nodes increases the computational time.

In contrast, the integration of Boundary Element Methods (BEM) with PD presents a promising opportunity to enhance the analysis of multi-scale crack propagation problems. BEM [32,33] inherently reduces the dimensionality of the problem by converting volume integrals into boundary integrals, resulting in significant computational savings, particularly for problems involving infinite domains [32]. When combined with PD, BEM can efficiently address non-local effects while maintaining a high level of detail near the crack tip, leveraging the strengths of both methods [34–36]. Early studies have demonstrated the practicality of this approach [37,38], showing that the efficiency of PD coupled with BEM is about ten times higher than PD coupled with FEM under the same computational condition [37]. However, the previous coupling strategy relied on domain decomposition and predefined crack domains, which do not reflect the realities of actual engineering applications. Thus, given the complexities involved in crack propagation phenomena and the limitations of existing methods, it is evident that employing adaptive coupling between PD and BEM is necessary for accurately and efficiently analyzing multi-scale crack propagation.

In this paper, an innovative multiscale crack propagation method is proposed based on the adaptive coupling between PD and BEM. By utilizing adaptive capabilities, one can dynamically refine the boundary element mesh in response to the evolving crack geometry and stress state. This approach can significantly improve computational efficiency without compromising the accuracy of the results. The highlights of the coupling method are as follows:

(1) The global structural deformation responses including macro-cracks are simulated using BEM with boundary elements only.
(2) A small square PD domain in 2D is defined exclusively at the crack tip with its geometry and discretization remaining unchanged throughout the analysis.
(3) The micro cracks' emergence, propagation, and transformation to macro cracks are accurately captured using PD.
(4) An adaptive iterative technique maintains the displacement continuity and force equilibrium, allowing BEM and PD to operate independently, without the need to compose an overall stiffness matrix.
(5) Various PD subdomains are not dependent on each other enabling parallel computation.
(6) This method aims to enhance computational efficiency while providing a robust framework for accurately analyzing multi-scale crack propagation problems.

The remainder of the paper is organized as follows: The formulation of bond-based PD and the dual boundary integral equation (BIE) formulation (Button-Miller BEM) for modeling cracks, along with the adaptive coupling multiscale approach, are outlined in section 2. Then, the verification of the accuracy of the proposed method and the numerical results are presented in section 3. Finally,

the paper is concluded in section 4.

## 2. Algorithm of adaptive coupling of PD and BEM

In this method, the bond-based PD (BBPD) theory and Button-Miller BEM are used to analyze the PD domain and BEM domain, respectively. A brief introduction to these two methods is presented below. Then, the adaptive coupling technique is detailed illustrated.

### 2.1. Bond-based peridynamic theory

This work focuses solely on the BBPD framework. A brief overview of the BBPD is provided, further details can be found in Ref. [39].

The fundamental equation of motion for any material point in BBPD is given by:

$$\rho\ddot{\mathbf{u}}(\mathbf{x},t)=\int_{H_x}\boldsymbol{f}[\boldsymbol{\eta},\boldsymbol{\xi},t]\boldsymbol{dV}_{\boldsymbol{x}'}+\boldsymbol{b}(\mathbf{x},t),\ \forall\mathbf{x}'\in H_x, \tag{1}$$

where $H_X$ denotes the neighborhood of point $\mathbf{x}$ ,it is typically defined as a spherical region with a radius $\delta$ centered at point $\mathbf{x}$. The variables $\ddot{\boldsymbol{u}}$ and $\rho$ represent the acceleration vector and mass density, respectively, which is consistent with the continuum mechanics. The vector $\mathbf{b}$ indicates the body force density. The response function $\mathbf{f}$, defined as a force vector per unit volume square. The initial relative position vector $\boldsymbol{\xi}$ between $\mathbf{x}$ and $\mathbf{x}'$ in the reference configuration and their current relative displacement vector $\boldsymbol{\eta}$ at time $t$ are provided below:

$$\boldsymbol{\xi}=\mathbf{x}'-\mathbf{x}\ \mathbf{and}\ \boldsymbol{\eta}=\boldsymbol{u}'(\mathbf{x}',t)-\boldsymbol{u}(\mathbf{x},t) \tag{2}$$

For a prototype micro-elastic brittle (PMB) material, the force function $\mathbf{f}$ can be expressed as [39]

$$\boldsymbol{f}(\boldsymbol{\eta},\boldsymbol{\xi})=\frac{\partial w(\boldsymbol{\eta},\boldsymbol{\xi})}{\partial\boldsymbol{\eta}}=\frac{\boldsymbol{\eta}+\boldsymbol{\xi}}{|\boldsymbol{\eta}+\boldsymbol{\xi}|}s(\boldsymbol{\eta},\boldsymbol{\xi})c(\boldsymbol{\xi},\delta)\mu,\ \forall\boldsymbol{\eta},\boldsymbol{\xi}, \tag{3}$$

where $w(\eta,\xi)=\frac{c(\xi,\delta)s(\eta,\xi)^2|\xi|}{2}$ is the micro-elastic potential. $s$ refers to the stretch of a bond, which relates to the strain in continuum mechanics and is expressed as

$$s(\boldsymbol{\eta},\boldsymbol{\xi})=\frac{|\boldsymbol{\eta}+\boldsymbol{\xi}|-|\boldsymbol{\xi}|}{|\boldsymbol{\xi}|} \tag{4}$$

$c$ is the micro-modulus, representing the stiffness of a pair of bonds. The micro-modulus $c$ is derived from the consistency between the strain energy density in PD theory and classical continuum theory as shown below:

$$\begin{gathered}c=\frac{12E}{\pi\delta^4},\ \text{3D}\\ c=\frac{9E}{\pi t_h\delta^3},c=\frac{48E}{5\pi t_h\delta^3},\ \text{2D plane stress},\ \text{plane strain},\\ c=\frac{2E}{A\delta^2},\ \text{1D}\end{gathered} \tag{5}$$

where $E$ is the macroscopic Young's modulus. A bond-breaking parameter $\mu(\xi,t)$ is defined as:

$$\mu(\xi,t)=\begin{cases}1,\ \text{if } s<s_0,\ \text{for all } 0\le t\\ 0,\ \text{otherwise}\end{cases} \tag{6}$$

Failure of the material occurs when the stretch $s$ reaches its critical value $s_0$:

$$\begin{gathered}s_0=\sqrt{\frac{5G_{IC}}{6E\delta}},\ \text{3D},\\ s_0=\sqrt{\frac{4\pi G_{IC}}{9E\delta}},s_0=\sqrt{\frac{5\pi G_{IC}}{12E\delta}},\ \text{2D plane stress},\ \text{plane strain}\end{gathered} \tag{7}$$

where $G_{IC}$ is the critical energy release rate for mode I fracture.

The rupture of the bond is irreversible, making the constitutive model history-dependent. The damage level $\varphi$ at a material point $\mathbf{x}$ at time $t$ is defined as:

$$\varphi(\boldsymbol{x},t)=1-\frac{\int_{H_x}\mu(\xi,t)dV_{\mathbf{x}'}}{\int_{H_x}dV_{\mathbf{x}'}},\ 0\le\varphi\le 1 \tag{8}$$

It should be noted that $\varphi=0$ represents the undamaged state and $\varphi=1$ is the complete separation of the single material point from all surrounding points within its horizon. In this analysis, we define that when $\varphi>0.38$, the micro crack transition to the macro crack.

To control the extent of crack propagation, the problems being addressed are modeled in a steady-state scenario. Therefore, the adaptive dynamic relaxation method introduced by Kilic [40] is used, in which the damping coefficient is adjusted adaptively at each time step. By eliminating the acceleration term and introducing a fictitious diagonal density and damping matrix that is proportional to the density matrix, Eq. (1) can be cast into a set of ordinary differential equations suitable for dynamic relaxation:

$$\Lambda\ddot{\boldsymbol{u}}(\boldsymbol{x},t)+c_n\Lambda\dot{\boldsymbol{u}}(\boldsymbol{x},t)=\boldsymbol{F}(\boldsymbol{u},\boldsymbol{u}',\boldsymbol{x},\boldsymbol{x}'), \tag{9}$$

in which, $\boldsymbol{\Lambda}$ represents the fictitious diagonal density matrix, while $c_n$ refers to the damping coefficient whose values are determined through Greschgorin's theorem and Rayleigh's quotient, respectively [40]. The vector $\mathbf{F}$ denotes the sum of internal and external force and its *ith* component can be written as

$$\boldsymbol{F}_i=\boldsymbol{b}(\boldsymbol{x}_i,t)+\boldsymbol{f}_i(\boldsymbol{\xi},\boldsymbol{\eta},t) \tag{10}$$

By utilizing the central-difference explicit integration, displacements and velocities for the next iteration step can be written as

$$\begin{aligned}\dot{\boldsymbol{u}}^{n+1/2}&=\left[(2-c_n\Delta t)\dot{\boldsymbol{u}}^{n-1/2}+2\Delta t\boldsymbol{\Lambda}^{-1}\boldsymbol{F}^n\right]/(2+c_n\Delta t),\\ \dot{\boldsymbol{u}}^n&=1/2\left(\dot{\boldsymbol{u}}^{n-1/2}+\dot{\boldsymbol{u}}^{n+1/2}\right)\\ \boldsymbol{u}^{n+1}&=\boldsymbol{u}^n+\Delta t\dot{\boldsymbol{u}}^{n+1/2}\end{aligned} \tag{11}$$

in which, $n$ indicates the $n$th time iteration. However, the integration algorithm given by Eq. (11) cannot be used to start the integration due to the unknown velocity field at $t^{-1/2}$. By assuming that $\boldsymbol{u}^0=0$ and $\dot{\boldsymbol{u}}^0=0$, integration can be started by using

$$\dot{\boldsymbol{u}}^{1/2}=\Delta t\boldsymbol{\Lambda}^{-1}\boldsymbol{F}^0/2 \tag{12}$$

The physical aspect of this algorithm is solely represented by the summation of internal and external forces, $\mathbf{F}$. The density matrix, damping coefficient, and time step size do not have to be physically meaningful quantities. Therefore, they can be selected to achieve faster convergence.

The damping coefficient for each iteration step can be expressed as:

$$\boldsymbol{c}_n=2\sqrt{\left((\boldsymbol{u}^n)^T\boldsymbol{K}^n\boldsymbol{u}^n\right)/\left((\boldsymbol{u}^n)^T\boldsymbol{u}^n\right)}, \tag{13}$$

in which, $\boldsymbol{K}^n$ is the diagonal "local" stiffness matrix, which is given

$$K_{ii}^n=-\left(f_i^n/\Lambda_i-f_i^{n-1}/\Lambda_i\right)/\left(\Delta t\dot{u}_i^{n-1/2}\right), \tag{14}$$

where, the diagonal density matrix, is expressed as

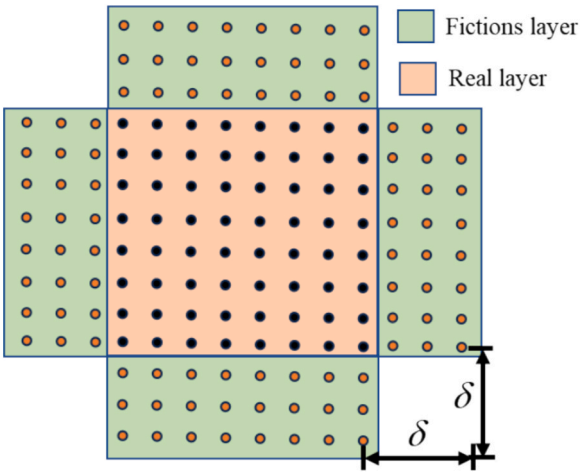


**Fig. 1.** PD domain discretization.

$$\Lambda_i = \frac{5}{4} dt^2 \frac{\pi \delta^2 hc}{dx}, \tag{15}$$

where 5 is a safe factor.

The numerical approximation of the PD equation starts with the subdivision of the structure into nodes. Each node is associated with a certain volume $V_j$, and the union of all volumes covers the entire body volume. Therefore, the discretized form of Eq. (1) is:

$$\rho \ddot{\boldsymbol{u}}(\boldsymbol{x}_i, t) = \sum_j \boldsymbol{f}(\eta, \xi, t) \upsilon_j V_j \mu\left(\left|\boldsymbol{\xi}_{ij}\right|, t\right) + \boldsymbol{b}(\boldsymbol{x}_i, t), \ \forall \boldsymbol{x}_j \in H_{\boldsymbol{x}_i} \tag{16}$$

where $\upsilon_j$ is the volume reduction factor. When the volume $V_j$ of node $j$ falls completely within the horizon of the central node $\mathbf{x}_i$, $\upsilon_j$ is equal to 1; and when $\delta - \Delta x/2 < \left|\boldsymbol{\xi}_{ij}\right| < \delta$, $\upsilon_j = \left(\delta + \Delta x/2 - \left|\boldsymbol{\xi}_{ij}\right|\right)/\Delta x$. In the discretized implementation, a regular grid of nodes is used. The grid spacing is the same in all directions ($\Delta x = \Delta y = \Delta z$). Then a cubic cell of volume $V_i = \Delta x^3$ (or a square cell of volume $V_i = \Delta x^2$) is associated with each node, which is placed at the center of the corresponding cell. Spatial integration is carried out using a single integration point. Boundary conditions are applied by imposing constraints on displacement and velocity fields within a "fictitious material layer", which has a depth of $\delta$, as illustrated in Fig. 1. The flowchart outlining the PD procedure is presented in Fig. 2.

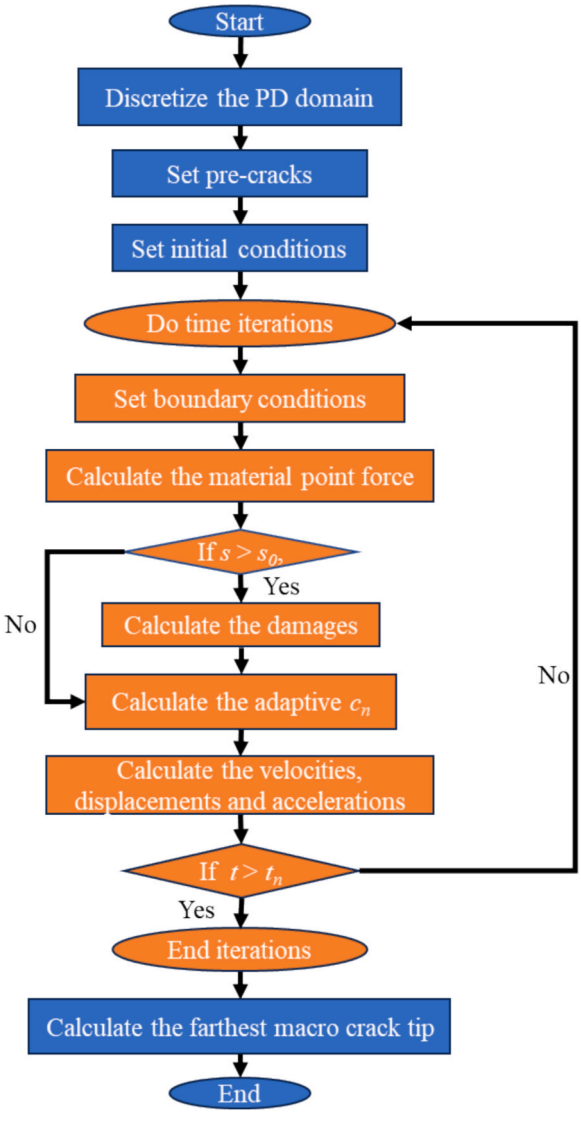


**Fig. 2.** The flowchart of the PD procedures.

### 2.2. Burton-Miller BEM

For more general cases, such as structures that contain both cracks and voids within a finite domain with loads applied on the outer boundary, it is necessary to apply general forms of both the displacement boundary integral equation (BIE) and traction BIE synchronously [34]. This combined approach is known as the dual BIE, which is used to solve such problems. The direct displacement BIE (also referred as the conventional BIE or CBIE) for a 2-D elastic body containing cracks is expressed as [32]:

$$\frac{1}{2}\boldsymbol{u}(\boldsymbol{x}) = \int_S [\boldsymbol{U}(\boldsymbol{x},\boldsymbol{y})\boldsymbol{t}(\boldsymbol{y}) - \boldsymbol{T}(\boldsymbol{x},\boldsymbol{y})\boldsymbol{u}(\boldsymbol{y})]dS(\boldsymbol{y}), \forall \boldsymbol{x} \in S, \tag{17}$$

where $\boldsymbol{S}$ represents the entire boundary of the problem domain which includes all crack surfaces as well as the outer boundary. **x** and **y** denote the source point and field point, respectively. **u** and **t** are the displacement and traction vector, respectively. **U** and **T** denote the displacement and traction kernels in the Kelvin's solution [32]. It is important to note that the surface is assumed as smooth at the source point **x**. For reference, the expressions for the two kernels (**U** and **T**) under plane strain conditions are provided in index notation [32]:

$$\begin{cases} U^*_{ij}(\boldsymbol{x},\boldsymbol{y}) = \dfrac{1}{8\pi(1-\nu)G}\left[(3-4\nu)\delta_{ij}\ln\left(\dfrac{1}{r}\right) + r_{,i}r_{,j}\right] \\ T^*_{ij}(\boldsymbol{x},\boldsymbol{y}) = \dfrac{-1}{4\pi(1-\nu)r}\left\{(1-2\nu)\left(n_i r_{,j} - n_j r_{,i}\right) + \left[(1-2\nu)\delta_{ij} + 2r_{,i}r_{,j}\right]r_{,l}n_l\right\} \end{cases}, \tag{18}$$

in which, $G$ is the shear modulus, $\nu$ is Poisson's ratio, $r$ is the distance between the source points **x** and field point **y**. $\delta_{ij}$ is the Kronecker symbol, and $n_i$ is the direction cosine of the normal.

Additionally, the direct traction BIE (hypersingular BIE or HBIE) is required as well [34]:

$$\frac{1}{2}\boldsymbol{t}(\boldsymbol{x}) = \int_S [\boldsymbol{K}(\boldsymbol{x},\boldsymbol{y})\boldsymbol{t}(\boldsymbol{y}) - \boldsymbol{H}(\boldsymbol{x},\boldsymbol{y})\boldsymbol{u}(\boldsymbol{y})]dS(\boldsymbol{y}), \forall \boldsymbol{x} \in S, \tag{19}$$

where **K** and **H** are the two new kernels in the Kelven's solution. The two kernels (**K** and **H**) for the case of plane strain are given in the following [34]:

$$\begin{aligned} K_{ij}(\boldsymbol{x},\boldsymbol{y}) &= \frac{1}{4\pi(1-\nu)r}\left[(1-2\nu)\left(\delta_{ij}r_{,k} + \delta_{jk}r_{,i} + \delta_{ik}r_{,j}\right) + 2r_{,i}r_{,j}r_{,k}\right]n_k(\boldsymbol{x}) \\ H_{ij}(\boldsymbol{x},\boldsymbol{y}) &= \frac{\mu}{2\pi(1-\nu)r^2}\left\{\begin{array}{c} 2\dfrac{\partial r}{\partial n}\left[(1-2\nu)\delta_{ik}r_{,j} + \nu\left(\delta_{ij}r_{,k} + \delta_{jk}r_{,i}\right) - 4r_{,i}r_{,j}r_{,k}\right] + 2\nu\left(n_i r_{,j}r_{,k} - n_k r_{,i}r_{,j}\right) \\ -(1-4\nu)\delta_{ik}n_j + (1-2\nu)\left(2n_j r_{,i}r_{,k} + \delta_{ij}n_k + \delta_{jk}n_i\right) \end{array}\right\}n_k(\boldsymbol{x}) \end{aligned} \tag{20}$$

Fig. 3 illustrates the most commonly used dual BIE approach in the literature for modeling cracks with two-surface models. In Fig. 3 (a), the displacement BIE (CBIE) is applied on one side of the crack, while the traction BIE (HBIE) is applied on the opposite side. The CBIE is also used on another non-crack surface. This dual BIE approach has been utilized in various studies to address crack propagation problems. Another dual BIE approach is known as the Burton and Miller BIE [34], which is depicted in Fig. 3 (b). This approach was originally developed to solve exterior acoustic wave problems to overcome the fictitious eigenfrequency difficulties in the BIEs. It uses a linear combination of the CBIE and HBIE as follows:

$$\alpha\text{CBIE} + \beta\text{HBIE} = 0, \tag{21}$$

where $\alpha$ and $\beta$ represent the coupling coefficients. This dual BIE formulation is applied to the entire boundary which includes all crack surfaces. It has proven to be effective in solving crack problems in both 3-D elastodynamics and 2-D elastostatics for calculating SIFs [34].

In this study, the Button-Miller BIE is employed, utilizing an adaptive coefficient which is proven to be more efficient than using a constant coefficient. The following formula is used to determine the value of each collocation point x:

$$\beta = \beta(\boldsymbol{x}) = \frac{h(\boldsymbol{x})}{E}, \tag{22}$$

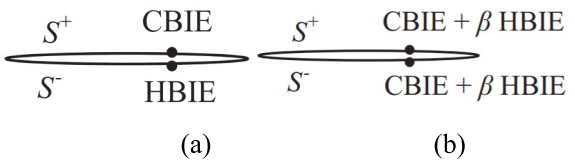


**Fig. 3.** Dual BIE approaches.

where $h(\mathbf{x})$ represents the size of the element associated with the collocation point $\mathbf{x}$ , and $E$ is Young's modulus.

Constant elements are utilized in the discretization of dual BIE for modeling cracks in 2-D. The constant elements may have lower accuracy compared to linear or quadratic elements, but they have shown the capability to produce precision in a variety of verification cases. The advantages of using constant elements include: (1) Ease of implementation: The analytical integration of all necessary integrals is available in the literature [30], which removes the need for numerical integration; (2) Satisfaction of smoothness requirements: The smoothness condition for the HBIE is met at the collocation points; and (3) Avoidance of corner problems: Constant elements simplify the modeling process by eliminating the need to address corner issues. The flowchart outlining the BEM procedures is listed in Fig. 4.

### 2.3. Coupling of PD and BEM

In the coupling approach, the global structure with macro cracks is simulated using the BEM model. Meanwhile, the crack tip region is modeled separately using the PD model. The BEM model is discretized with boundary constant elements, while the PD model is discretized with material points, as shown in Fig. 5. It is important to note that there are no common nodes between the two models.

The displacement continuity and force equilibrium conditions are used to couple these two domains together. The displacements at the BEM interfaces are subjected to the corresponding fictitious layers of PD domain using Eq. (23) (Fig. 6). The interacting forces between virtual PD nodes and real PD nodes are used to calculate the anti-force at the BEM interfaces by Eq. (24). It is important to note that interactions among virtual PD nodes are not considered as anti-forces (See Fig. 6).

$$u_i^{BEM} = u_{i1}^{FM} = u_{i2}^{FM} = u_{i3}^{FM}, \tag{23}$$

$$t_i^{BEM} = -\left(f_{1j}^{FM} + f_{2j}^{FM} + f_{3j}^{FM}\right) \cdot dx \tag{24}$$

#### 2.3.1. An adaptive iterative Algorithm 1

An adaptive iterative algorithm is developed to keep balance between the BEM and PD interfaces. The details of Algorithm 1 are listed below:

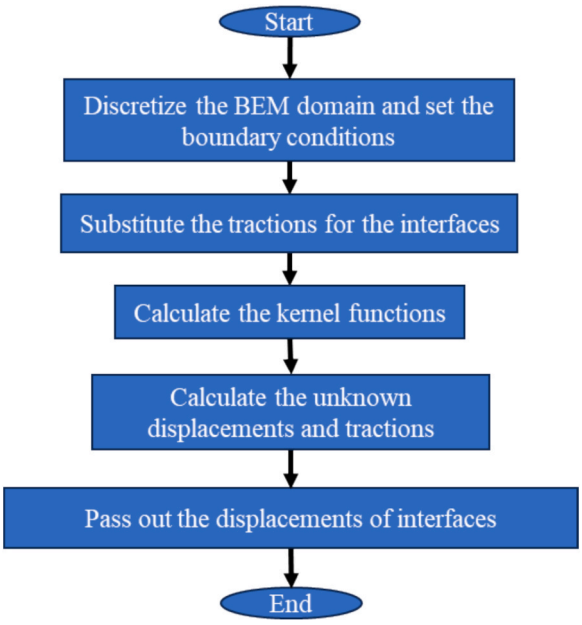


**Fig. 4.** Flowchart of BEM procedures.

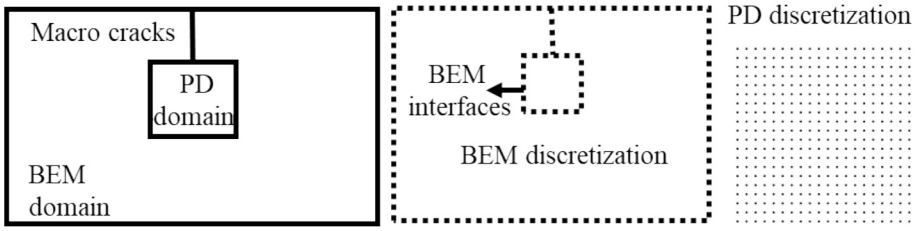


**Fig. 5.** Coupling model.

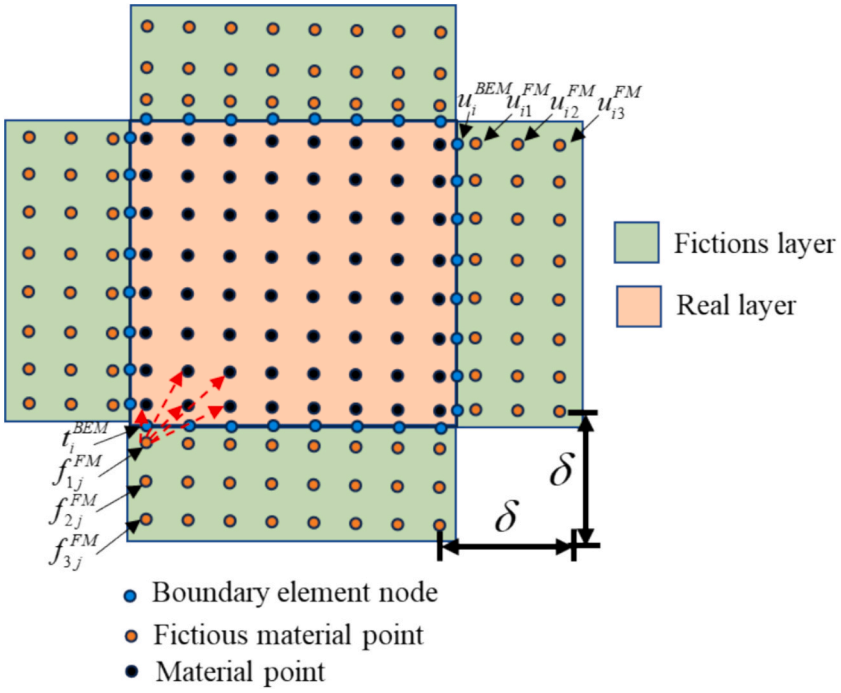


**Fig. 6.** Displacement continuity and force equilibrium at interfaces.

**Algorithm 1.** (*Iteration between BEM domain and PD domain*)

1) *Set the displacement boundary condition for the interfaces in the PD domain* $\boldsymbol{u}_{IPD}^{n} = 0$;
2) *Use the BBPD algorithm to calculate the force of the PD domain;*
3) *Substitute the anti-force of the interfaces calculated from PD as the boundary condition to calculate the BEM domain by BIE.* $\boldsymbol{t}_{IBEM}^{n} = -\boldsymbol{f}_{IPD}^{n} \times dx$.
4) *Obtained the interface displacements from BEM calculation* $\boldsymbol{u}_{IBEM}^{n}$.
5) *Evaluate the errors between* $\boldsymbol{u}_{IBEM}^{n}$ *and* $\boldsymbol{u}_{IPD}^{n}$ *by* $\frac{\boldsymbol{u}_{IBEM}^{n} - \boldsymbol{u}_{IPD}^{n}}{\boldsymbol{u}_{IBEM}^{n}} = e$.
6) *If* $e < \psi$ *or* $n_{iterative} > n_{\max}$, *end the iteration. Otherwise, apply a gradient descent technique to update the displacement based on the previous displacement of BEM and PD.* $\boldsymbol{u}_{IPD}^{n} = w_n \times \boldsymbol{u}_{IBEM}^{n-1} + (1 - w_n) \times \boldsymbol{u}_{IPD}^{n-1}$.

*where Ψ is the user-defined error allowance. To enhance the rate of convergence, a relaxation of the displacement data along the interface can be applied in the next iteration* [41]. *Thus,*

$$\boldsymbol{u}_{IPD}^{n} = w_n \times \boldsymbol{u}_{IBEM}^{n-1} + (1 - w_n) \times \boldsymbol{u}_{IPD}^{n-1}, \tag{25}$$

where $w$ is the relaxation parameter subject to the constraint $0 < w \leq 1$. There is an infinite range of values that can be used for the relaxation parameter within the constraint region, only one value is optimum. The optimal $w$ is determined by minimizing the square error function of the interfacial displacements between the next and current iterations (Eq. (26)). In essence, the iterative procedure can be improved by allowing the relaxation parameter to adjust dynamically with each iteration.

$$\left\| \boldsymbol{u}_{IPD}^{n+1}(w) - \boldsymbol{u}_{IPD}^{n}(w) \right\|^2 \tag{26}$$

Then, minimizing it with respect to the relaxation parameter $w$ to determine the optimal dynamic value for the next iteration

$$w = \frac{\boldsymbol{e}_{IPD}^{n} \cdot \left(\boldsymbol{e}_{IPD}^{n} - \boldsymbol{e}_{IBEM}^{n}\right)}{\left(\boldsymbol{e}_{IPD}^{n} - \boldsymbol{e}_{IBEM}^{n}\right)^2}, with\, n \geq 2\, and\, 0 < w \leq 1, \tag{27}$$

where

$$\boldsymbol{e}_{IPD}^{n} = \boldsymbol{u}_{IPD}^{n} - \boldsymbol{u}_{IPD}^{n-1}\ and\ \boldsymbol{e}_{IBEM}^{n} = \boldsymbol{u}_{IBEM}^{n} - \boldsymbol{u}_{IBEM}^{n-1} \tag{28}$$

When applying this algorithm, it is essential to ensure that the PD and BE subdomains are well behaved and solvable during the decomposition process. The chart for algorithm 1 is plotted in Fig. 7

### 2.3.2. *Adaptive iteration Algorithm 2*

As the iteration progresses, corresponding displacement loads are subjected to the PD domain, leading to crack propagation. An adaptive crack propagation iteration algorithm has been developed to track both the crack propagation path and the transition of micro cracks, as well as the movement of the crack tip. It is important to note that a gradual load increment is applied to control the crack propagation process. This approach helps prevent the crack propagation length from exceeding the computational domain during a single load step, which could result in inaccurate calculations. The detailed procedure for iteration algorithm 2 is explained below and the flowchart is described in Fig. 8.

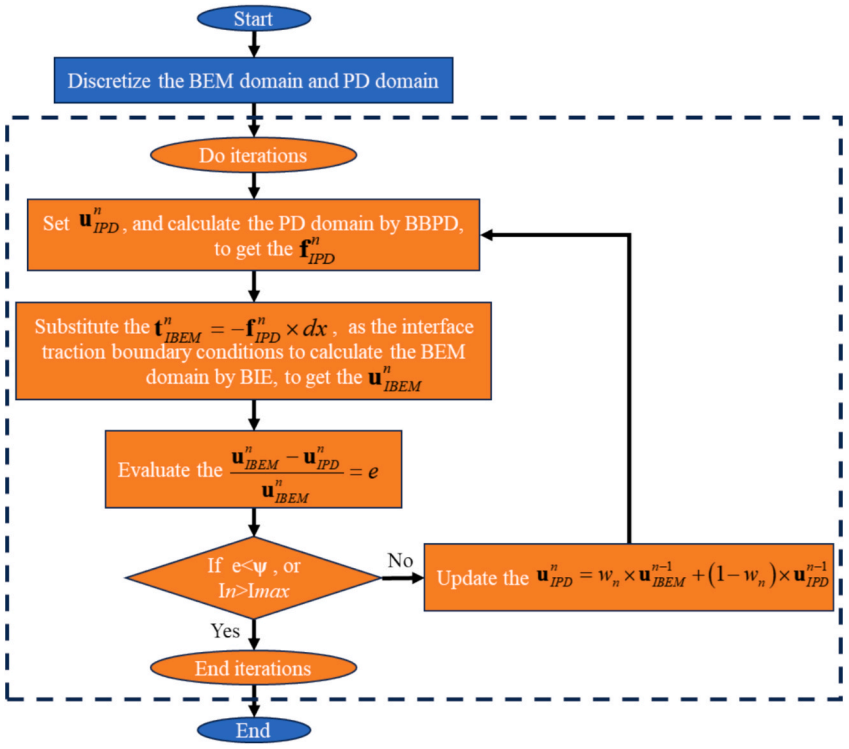


**Fig. 7.** Flow chart of Algorithm 1.

1) Perform crack propagation iterations;
2) Conduct load step iterations;
3) Increase the load for each load step;
4) Implement the iterative process of Algorithm 1;
5) Assess the relationship between the crack propagation length and the boundaries of the PD domain;
6) If the crack propagation length exceeds any 0.9 ratios of the boundary of the PD domain, end the load step iteration; If not, return to step 2);
7) Determine the moving distance of new PD domain;
8) Evaluate the relationship between crack propagation length and the overall structural boundaries.
9) If the crack propagation length exceeds any boundary of the whole structure, then the structure fails, end the crack propagation iteration.
10) If not, adjust the macro-crack boundaries of the BEM domain, and relocate the PD domain; Set the current load, and the initial cracks of the new PD domain, and return to step 1;

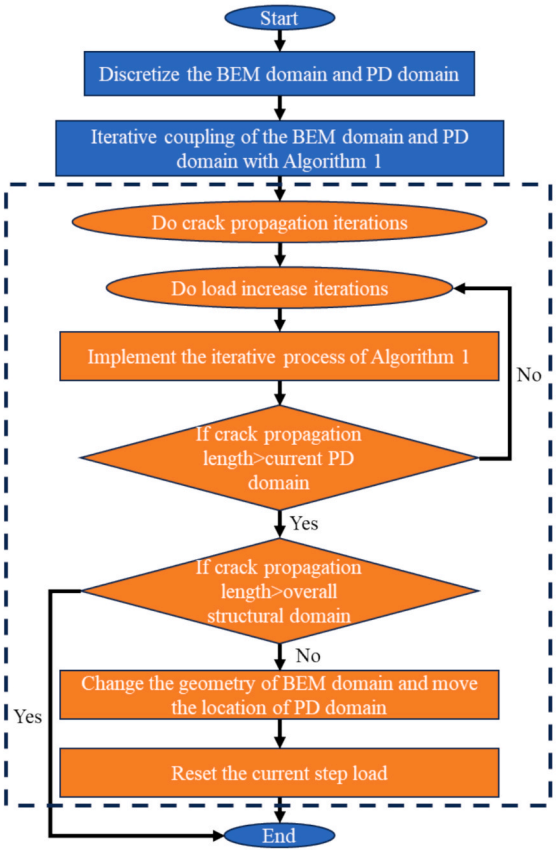


**Fig. 8.** Flowchart of iterative Algorithm 2.

**Algorithm 2.** (*Crack propagation iteration*)

1) *Perform crack propagation iterations*;
2) *Conduct load step iterations*;
3) *Increase the load for each load step*;
4) *Implement the iterative process of* Algorithm 1;
5) *Assess the relationship between the crack propagation length and the boundaries of the PD domain*;
6) *If the crack propagation length exceeds any* 0.9 *ratios of the boundary of the PD domain, end the load step iteration*; *If not, return to step* 2);
7) *Determine the moving distance of new PD domain*;
8) *Evaluate the relationship between crack propagation length and the overall structural boundaries.*
9) *If the crack propagation length exceeds any boundary of the whole structure, then the structure fails, end the crack propagation iteration.*
10) *If not, adjust the macro-crack boundaries of the BEM domain, and relocate the PD domain*; *Set the current load, and the initial cracks of the new PD domain, and return to step* 1;

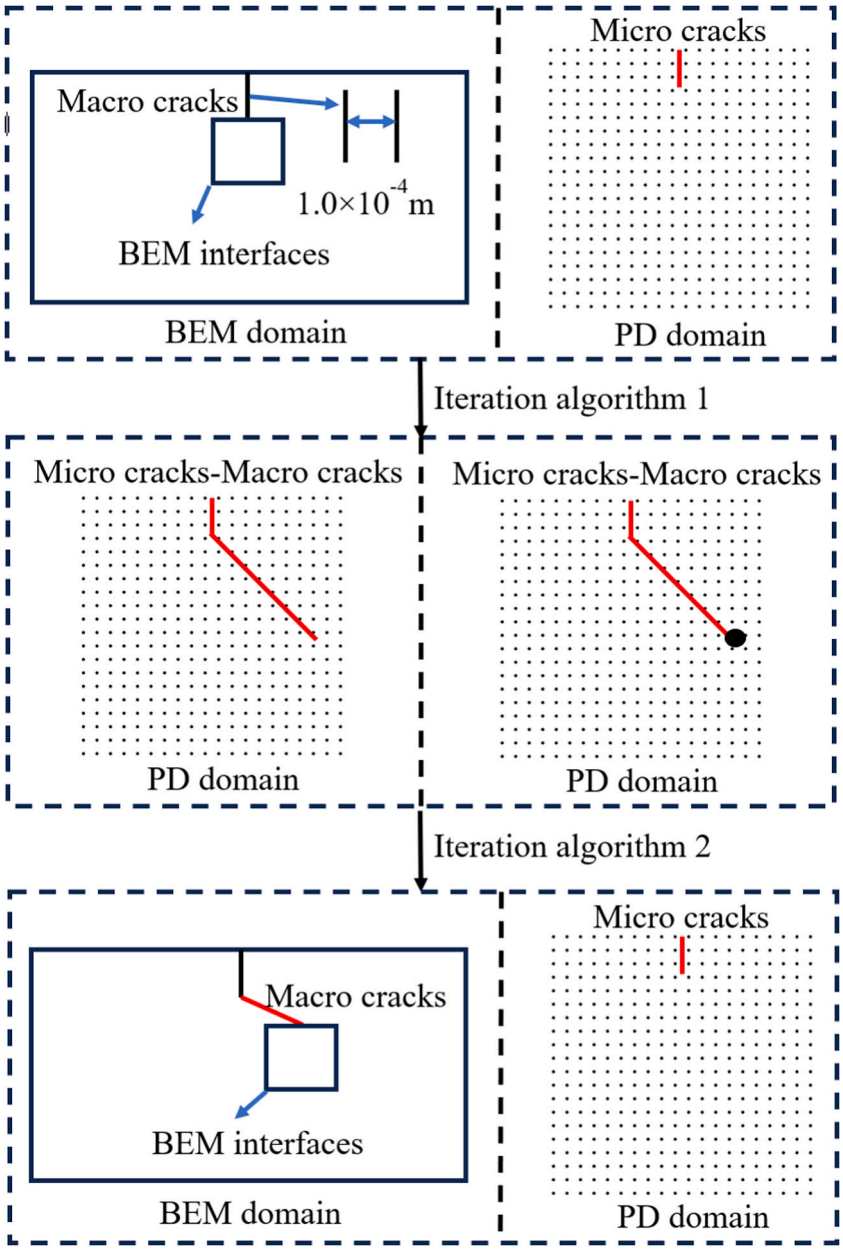


**Fig. 9.** Geometry iteration process.

#### 2.3.3. Geometry iteration

In the initial BEM model, the macro cracks are represented as two free edges with a gap $1.0 \times 10^{-4}$m. An initial crack with a length equal to 0.2 times the edge length of PD is established within the PD domain. An iterative algorithm 1 is applied to achieve a equilibrium between BEM and PD models. Following, the iterative Algorithm 2 is used to trace the crack propagation behaviors and identify the farthest crack tip. When the crack extends to 0.9 times the length and width of the PD domain, the current computational step is interrupted to modify the BEM model. The macro crack grows to reach the farthest macro crack tip identified in the PD domain at the previous step. The new macro crack edges are then discretized using an appropriate number of boundary elements, and the location of the BEM interfaces is adjusted accordingly. Throughout this computational process, the geometry and the discretization of the PD domain remain unchanged. Detailed geometry iterations are illustrated in Fig. 9.

## 3. Numerical analysis

The adaptive coupling method that has been developed is implemented using a Fortran program. First, the accuracy and efficiency of the present method are verified through a series of testing examples. Then, this method is used to analyze multi-scale crack propagation problems.

### 3.1. Verification

In this section, the intact and defective beams and plates with various coupling schemes are established to test the accuracy and efficiency of the present method. The results are compared with those obtained through analytical or other numerical methods.

#### 3.1.1. A cantilever beam subjected to tension

A cantilever beam with a length of 1 m and a height of 0.2 m is being analyzed. Material properties are $E = 100$ GPa, $\rho = 7850$ kg/m$^3$, and $\nu = 1/3$. Half of the beam is discretized using boundary elements, while the other half is discretized with material points. The schematic representation of this model is illustrated in Fig. 10. In the PD dynamic relaxation analysis, the time step is set to 1.0 s, with a total of 6000 steps. A constant relaxation factor of 0.4 is applied in the gradient descent technique outlined in Algorithm 1. The final convergence criterion is set at $\Psi = 1 \times 10^{-2}$ m. Throughout the analysis, the iterative steps for all models do not exceed 15 steps.

Four discretized models were constructed, each with varying numbers of boundary elements and material points. The specific counts for boundary elements and material points are detailed in Table 1 and illustrated in Fig. 11. The displacement contours in both $x$ and $y$ directions for each model are depicted in Fig. 12. It is evident that the displacement distributions are smooth and continuous, even for model 1, which has fewer boundary elements and material points. There are no noticeable jumps at the interfaces. Due to the characteristics of discretization, a low number of boundary elements and material points can result in inconsistencies in the geometry. However, this issue is resolved as the density of boundary elements and material points increases.

To verify the accuracy of the results. The central line displacements are collected for comparing with the analytical solutions. For each model in the BEM domain, 9 internal nodes were distributed to obtain the central line displacements without affecting the accuracy of the BEM. The central line displacements of the four models are illustrated in Fig. 13. These displacements closely match the analytical solutions, even at the interfaces, demonstrating the analyzed results are sufficiently accurate, even with small boundary elements and material points. There are only minor differences were observed in the PD domain. However, increasing the number of elements and points will decrease these differences.

#### 3.1.2. A cantilever beam subjected to shear forces

The cantilever beam designed for tensile loading has been modified to function as a shear loading beam by substituting a point load at the top of the right edge, as shown in Fig. 14. The geometry and material properties remain unchanged. Five discretized models, along with their respective displacement contours are depicted in Fig. 15 and Fig. 16. Detailed information about these five models is provided in Table 2. Internal points are also utilized to collect the central line displacements. The central line displacements are plotted in Fig. 17. It is concluded that increasing the number of boundary elements and material points enhances the accuracy at the interfaces.

The central line displacements closely match the analytical solutions, even with small boundary elements and material points. There are only minor differences observed in the PD domain. However, increasing the number of elements and points will reduce the differences.

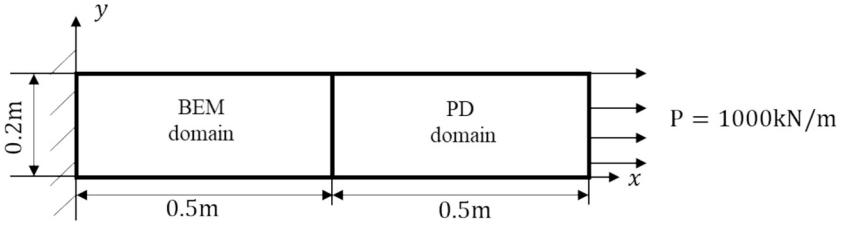


**Fig. 10.** The schematic of a tensile cantilever beam.

**Table 1**
The detailed distribution of a tensile cantilever beam.

| Models | BEM | | PD | |
|---|---|---|---|---|
| | No. of BEs in $x$ | No. of BEs in $y$ | No. of points in $x$ | No. of points in $y$ |
| 1 | 25 | 10 | 25 | 10 |
| 2 | 50 | 20 | 50 | 20 |
| 3 | 100 | 40 | 100 | 40 |
| 4 | 500 | 200 | 50 | 20 |

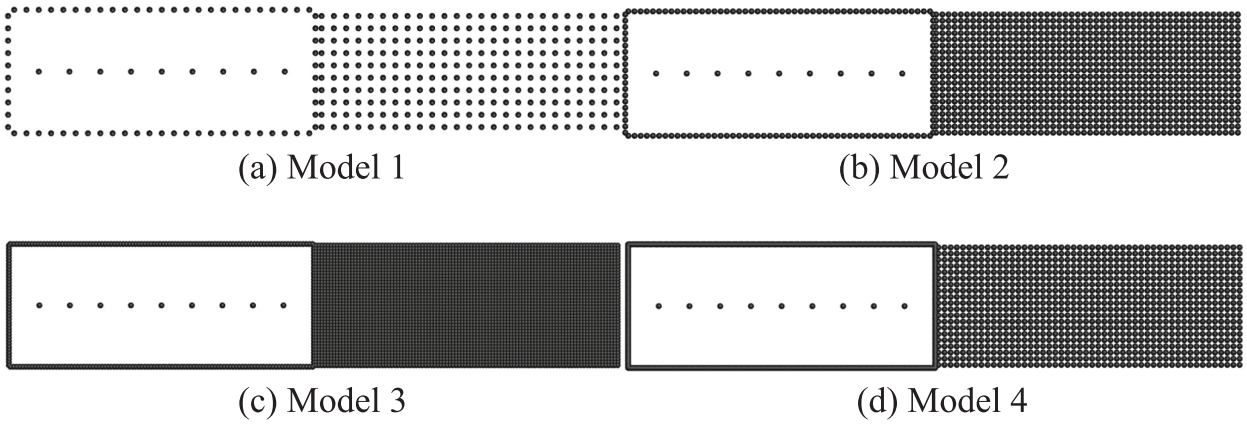


**Fig. 11.** Discretized models of a tensile cantilever beam.

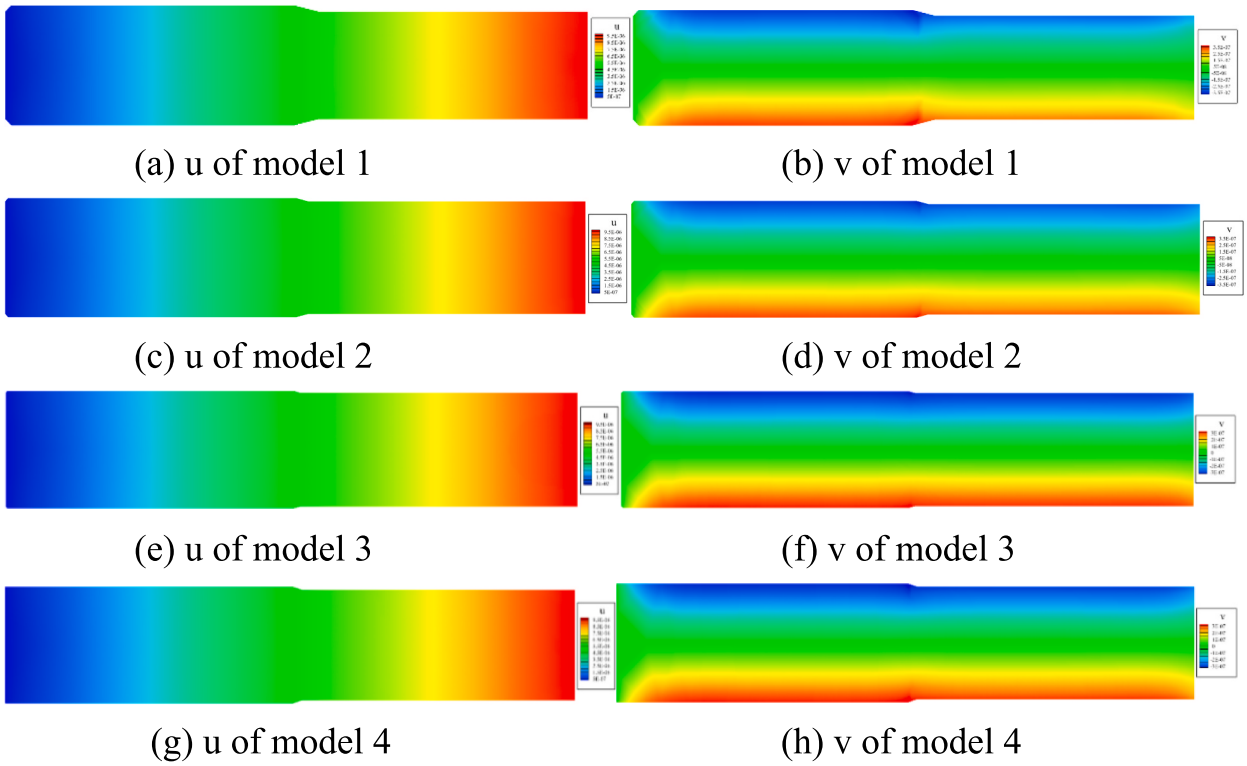


**Fig. 12.** Displacement contours of four discretization models.

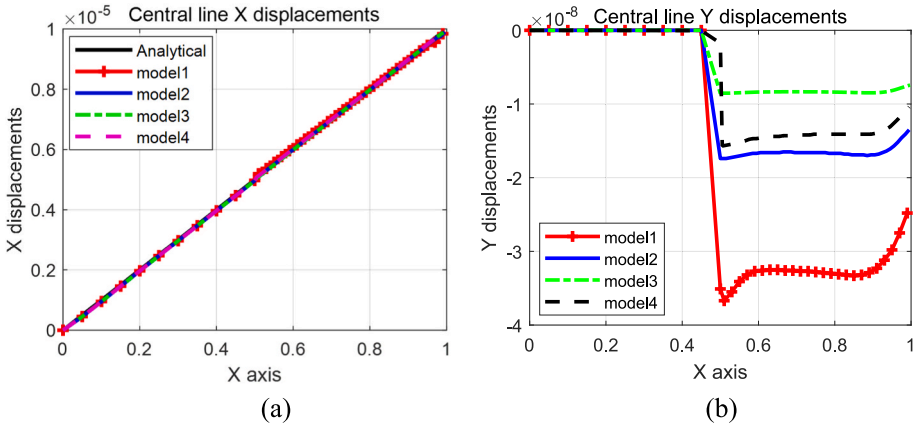


**Fig. 13.** Central line displacements comparison of a tensile cantilever beam.

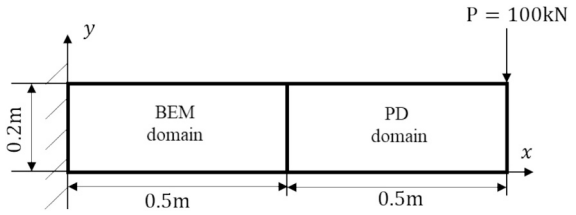


**Fig. 14.** The schematic of a shear cantilever beam.

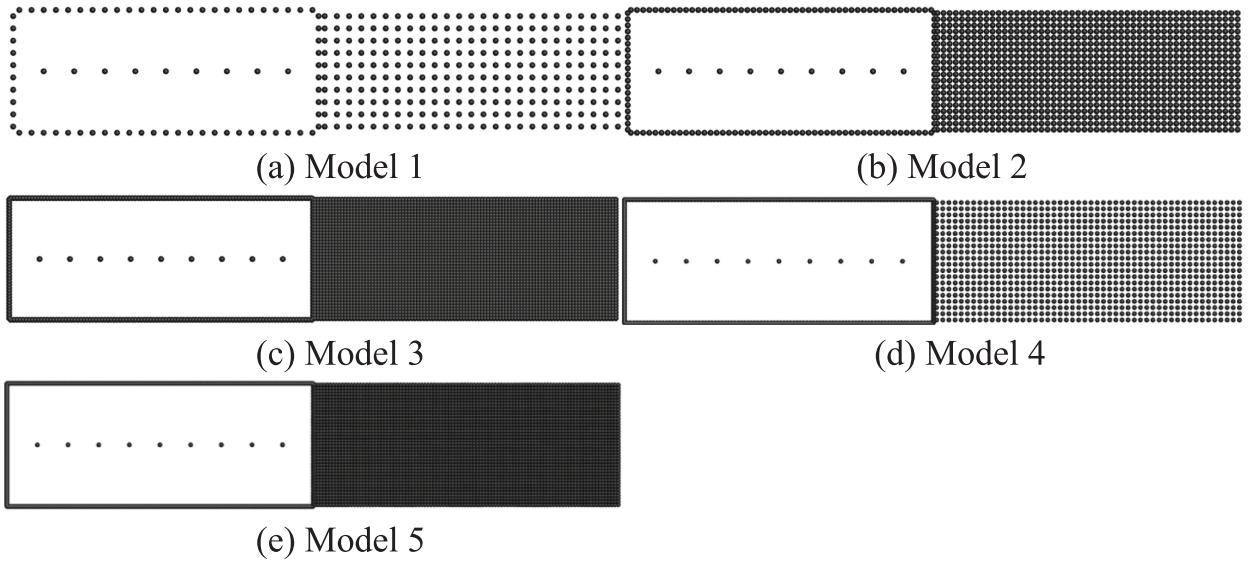


**Fig. 15.** Five discretization models of a shear cantilever beam.

### *3.1.3. A plate subjected to tensile loading*

To assess the impact of lessening the PD domain on the accuracy of the multi-scale models, a plate subjected to tensile loading described in Fig. 18 is simulated using the multi-scaled method with varying positions and PD domains. Material properties are $E = 100$ GPa, $\rho = 7850$ kg/m$^3$, and $\nu = 1/3$. A small PD square domain with a length of 0.1 m is placed at different positions within the macro BEM model. The detailed discretization models are illustrated in Fig. 19. The time step for the PD dynamic relaxation is set to 1.0 s, with a total of 1500 steps. A constant relaxation factor of 0.3 is used in the gradient descent technique outlined in Algorithm 1. The final convergence criterion is set at $\Psi = 1 \times 10^{-2}$ m. In the analysis, the number of iterative steps for all the models does not exceed 15 steps.

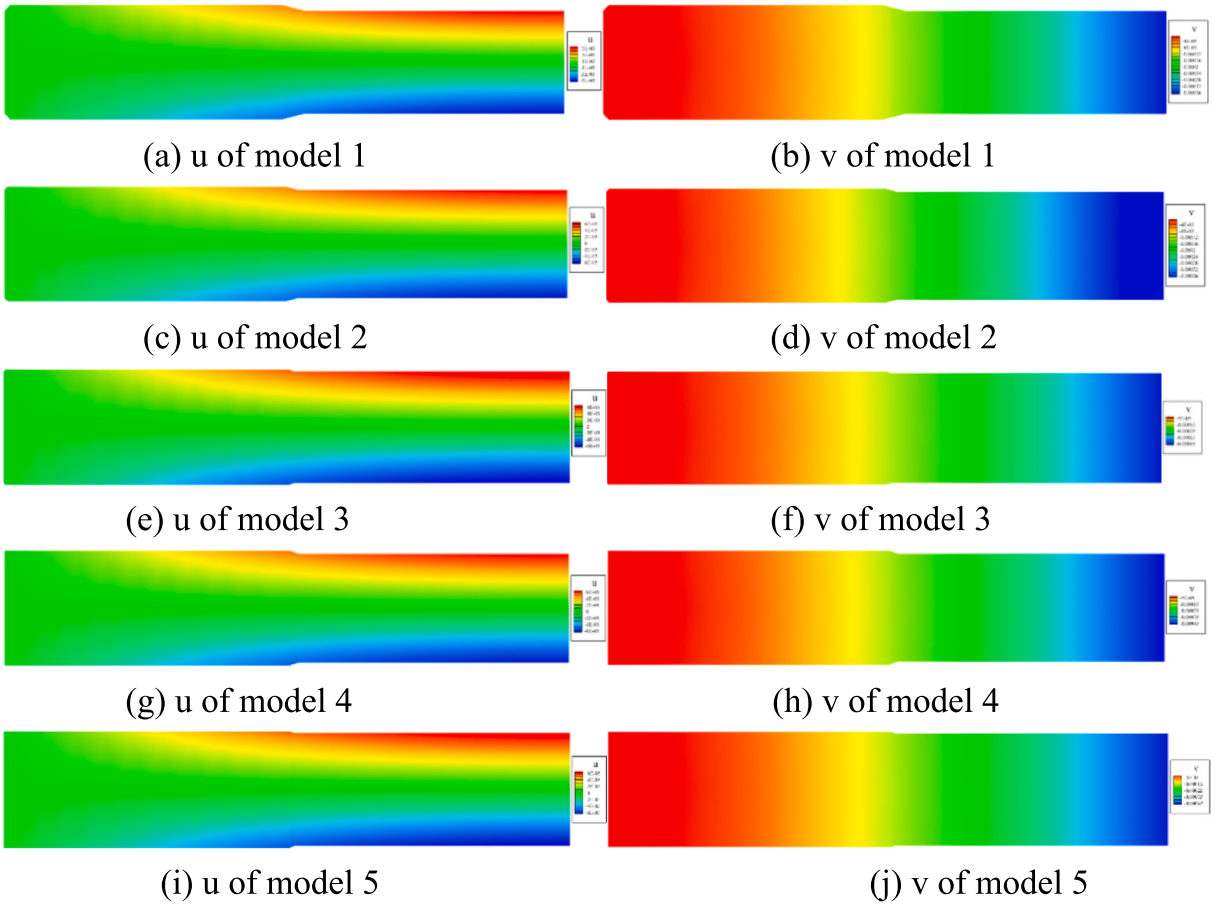


**Fig. 16.** Displacements contours of five discretization models.

**Table 2**
The detailed distribution of a shear cantilever beam.

| Models | BEM | | PD | |
|---|---|---|---|---|
| | No. of BEs in $x$ | No. of BEs in $y$ | No. of points in $x$ | No. of points in $y$ |
| 1 | 25 | 10 | 25 | 10 |
| 2 | 50 | 20 | 50 | 20 |
| 3 | 100 | 40 | 100 | 40 |
| 4 | 500 | 200 | 50 | 20 |
| 5 | 500 | 200 | 100 | 40 |

In this example, 340 constant elements are discretized within the macro BEM domain with an element interface of 0.01 m. Three different PD models are investigated, as shown in Fig. 19. The first model features a square PD configuration located at the center of the BEM domain. The second model shifts the square PD configuration 0.1 m to the left and upwards. The third model involves rotating the square PD domain by 45 degrees. A total of 400 material points is used to discretize the PD domain. The contours of the displacement distribution for these three models are depicted in Fig. 20. It can be observed that the displacement distribution is continuous, with only minor discontinuities occurring at the top corners of the square areas.

The accuracy at the edges of the square PD domain was compared with the analytical solutions. The results of error analysis for these three models are plotted in Fig. 21. It can be obtained that, the errors are a little big at the four corner points. This may be due to the use of constant elements in the BEM model, which may hinder precise measurement at the corners. However, increasing the number of boundary elements can reduce these errors.

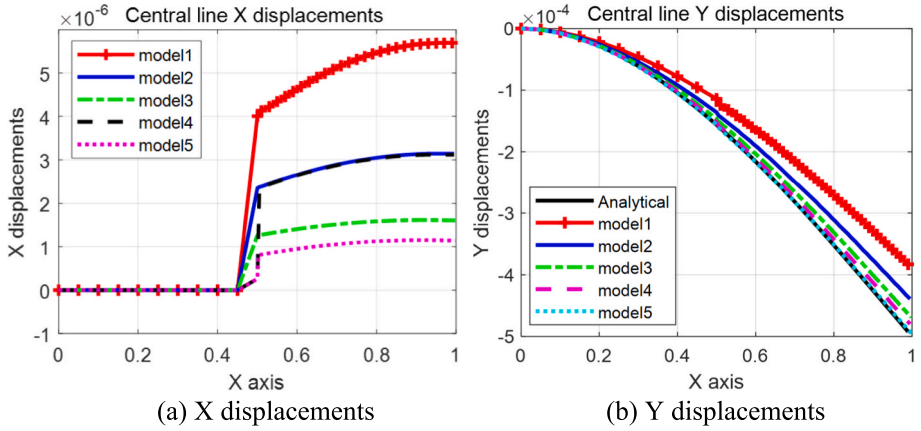


**Fig. 17.** Central line displacements comparison of five discretization models.

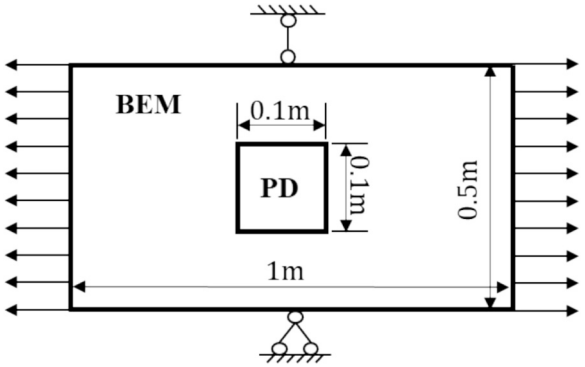


**Fig. 18.** a schematic of a tensile plate.

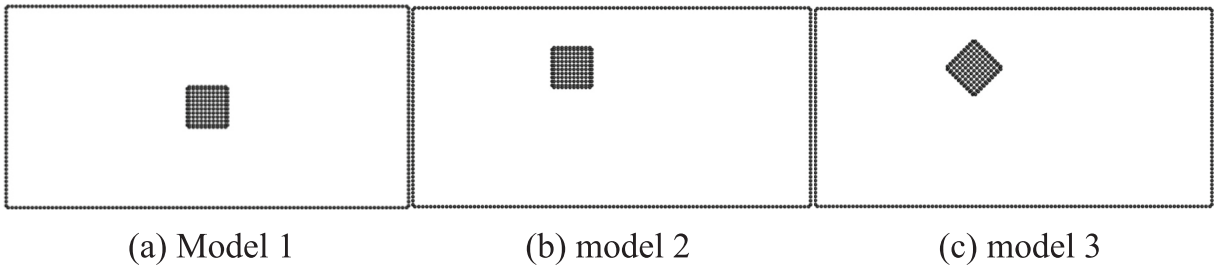


**Fig. 19.** Three discretization models of a tensile plate.

### 3.2. Crack propagation analysis

#### 3.2.1. A tensile plate with a pre-crack

The accuracy of crack propagation analysis is thoroughly examined. A plate measuring 20 m in length and 10 m in width is subjected to a distributed tensile loading along the left and right edges. The analysis focuses on an edge crack with varying crack length, specifically a width-to-crack length ratio a/w = 0.2, 0.5, and 0.8, which are analyzed by the present multi-scale crack propagation method. A micro square PD region with 2 m in length concentrates specifically on the crack tip. The material properties are $E = 1.0 \times 10^4$ Pa, $\nu = 1/3$. The schematic geometry of these three models is plotted in Fig. 22.

For different crack lengths, the geometry of BEM model varies, while it remains consistent for the PD model. For a crack length ratio of a/w = 0.2, the macro structure is discretized using BEM with 700 boundary elements. Each side of PD domain is discretized into 20 material points with a total of 400 points. When the crack length ratio is a/w = 0.5, the macro structure is discretized by BEM with 760 boundary elements, while the PD domain remains the same, also with 400 material points. A constant relaxation factor of 0.1 is used in the gradient descent in Algorithm 1 for both a/w = 0.2 and 0.5. For a crack length ratio of a/w = 0.8, the macro structure is discretized

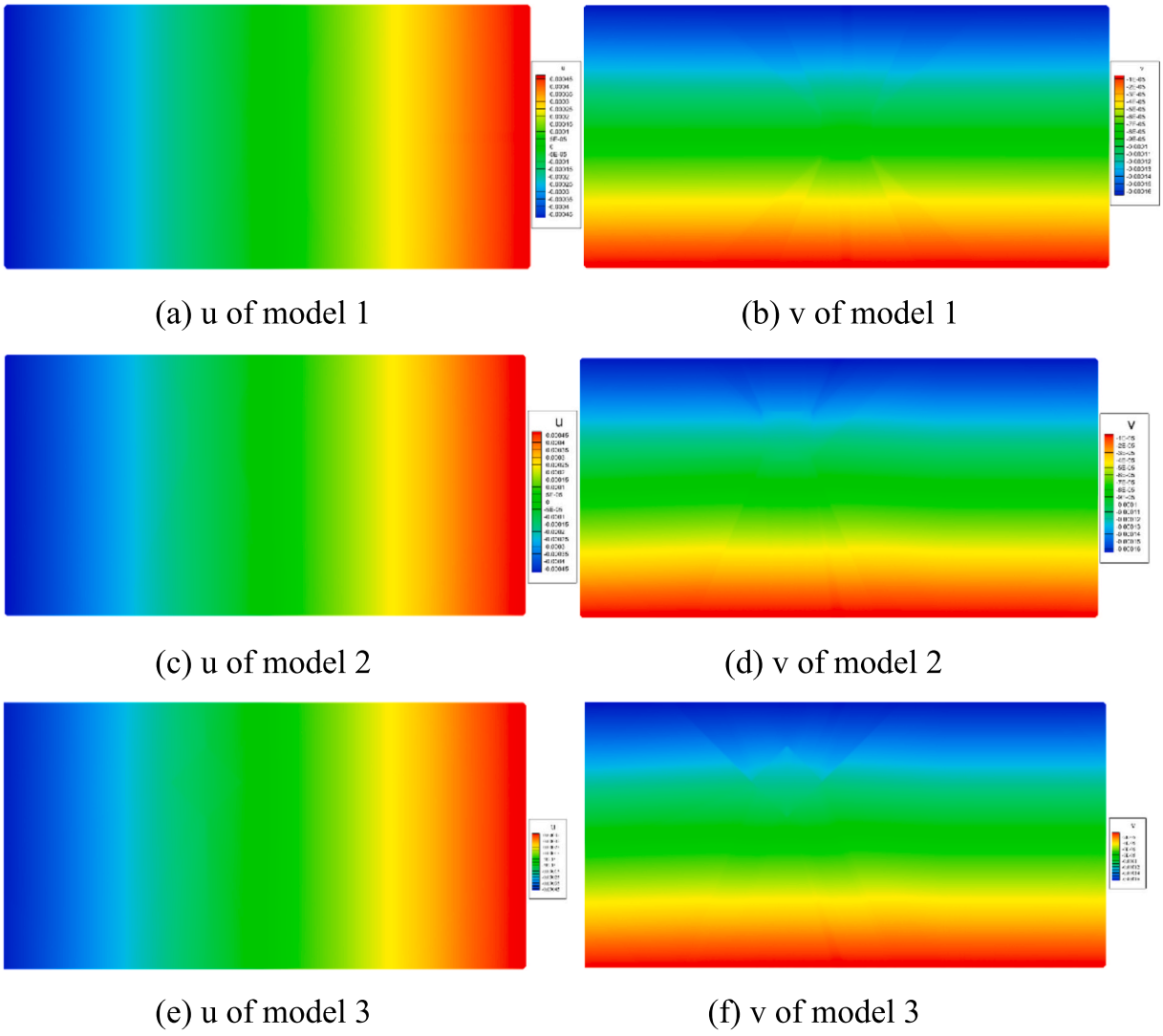


**Fig. 20.** Displacement contour of three discretization models for the tensile plate.

by BEM with 3680 boundary elements. Each side of PD domain is discretized into 40 material points with a total of 1600 points. A constant relaxation factor of 0.06 is accepted in the gradient descent in Algorithm 1. The detailed discretization model is plotted in Fig. 23. The time step in PD dynamic relaxation is set to 1.0 s, with a total of 1200 steps. The final convergence is $\Psi = 1 \times 10^{-2}$ m. In the analysis, the iterative steps for all models do not exceed 15 steps. Using the multi-scale crack propagation method, the displacement distributions of these three models are illustrated in Fig. 24.

The results of these three models are compared with analytical results and BEM results that involve only boundary elements. The corresponding errors, iterative steps and execution times are listed in Table 3. It can be observed that, the error for BEM is relatively smaller than that of PD-BEM coupling method when the aspect ratio is a/w = 0.2. However, for a/w = 0.5 and 0.8, the errors for BEM are larger than those for PD-BEM. This observation suggests that, when a/w = 0.2, the geometry for BEM is relatively regular. As the crack length propagates, the geometry for BEM becomes more extreme. Particularly at a/w = 0.8, only minimal connections are maintained, which increases the challenge for BEM and leads to less accuracy results. In contrast, this situation improves with the PD-BEM coupling method. Although the crack length increases, the interfaces of the BEM domain remain unchanged, allowing the geometry of BEM to adjust while the geometry of PD remains consistent throughout all computational steps. Consequently, even though the number of BEM elements increases by a factor of 5 and the number of material points increases by a factor of 4, the overall calculation time experiences only a slight increase.

To investigate the effects of the discretization on the accuracy of the present method. Three models with varying numbers of boundary elements and material points were analyzed for a/w = 0.5 and listed in Table 4. The results shown in the table indicate that the accuracy of the present method remains high, even with coarse discretization. Optimizing the discretization can enhance both the accuracy and the convergence factor. It is evident that, with the same number of boundary elements, a model with four times as many

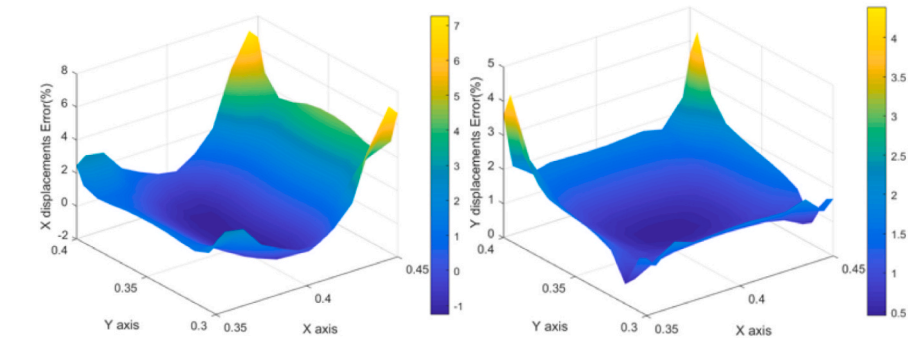


(a) u errors of PD domain in model 1 (b) v errors of PD domain in model 1

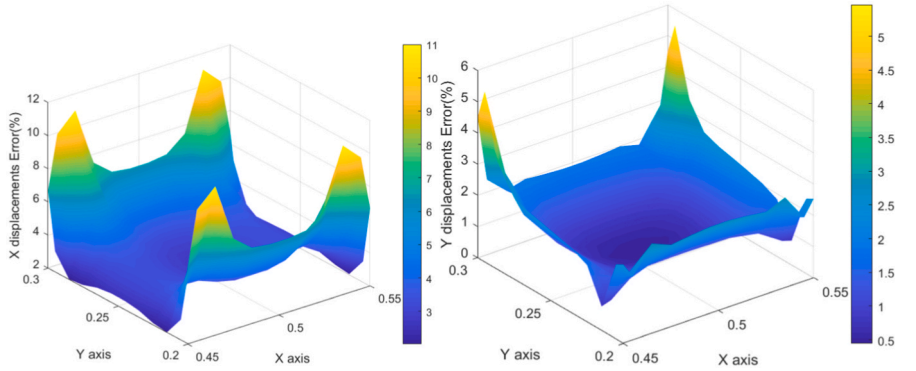


(c) u errors of PD domain in model 2 (d) v errors of PD domain in model 2

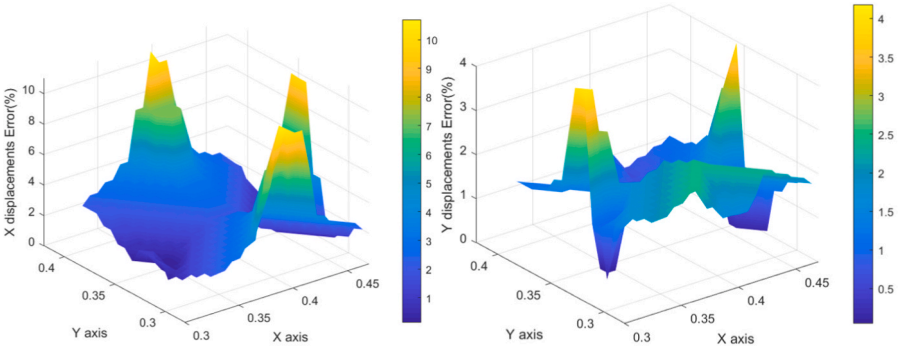


(e) u errors of PD domain in model 3 (f) v errors of PD domain in model 3

**Fig. 21.** Displacement errors in PD domain of three discretization models.

material points requires twice as much execution time.

Different discretization models have been investigated for the model with a crack length ratio of a/w = 0.8, and detailed results are listed in Table 5. When the crack is very close to the boundary of the structure, it can lead to extreme geometry. Optimizing the structural discretization will improve the accuracy of the results as well as the convergence factors, however, it will increase the execution time.

### *3.2.2. Crack propagation in a tensile plate*

In this example, a plate with an edge crack, as shown in Fig. 25, is studied by the present multi-scale method. The plate measures 20 m in length and 10 m in width, with an edge crack that extends 2 m along the top edge. The left edge of the plate is fixed, while a tensile load is subjected to the right edge. The initial load is set at 3.3 Pa with a load step size of 0.05 Pa. The Young's modulus of the plate is $1 \times 10^3$ Pa, $\nu = 1/3$. An initial macro-BEM model consists of 700 boundary elements, while a fixed PD model with 20 material points on each side, resulting in a total of 400 material points at the crack tip. Adaptive dynamic relaxation is applied with a time step of 1.0 s for a total of 1000 steps. The moving distance of PD domain is 0.5 m for each geometry iteration, and 5 boundary elements are added to each edge of the growing macro crack. The final convergence criterion is set at $\Psi = 1 \times 10^{-2}$ m. The adaptive relaxation parameter used

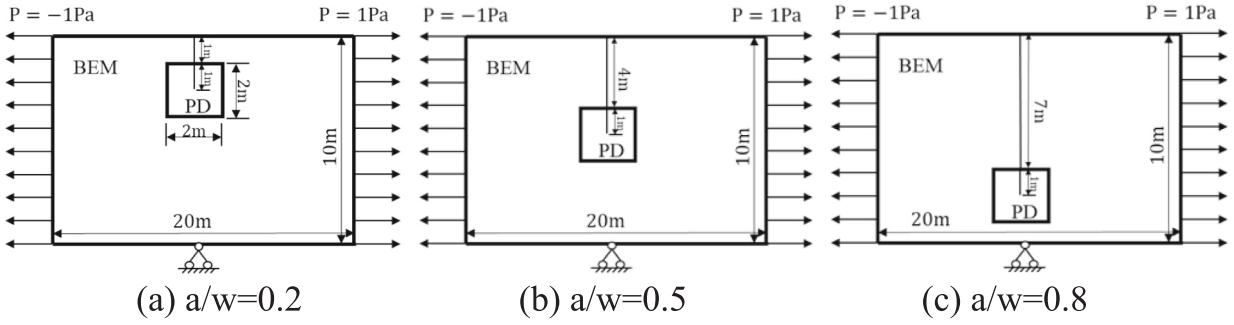


**Fig. 22.** The schematic of a tensile plate with a crack.

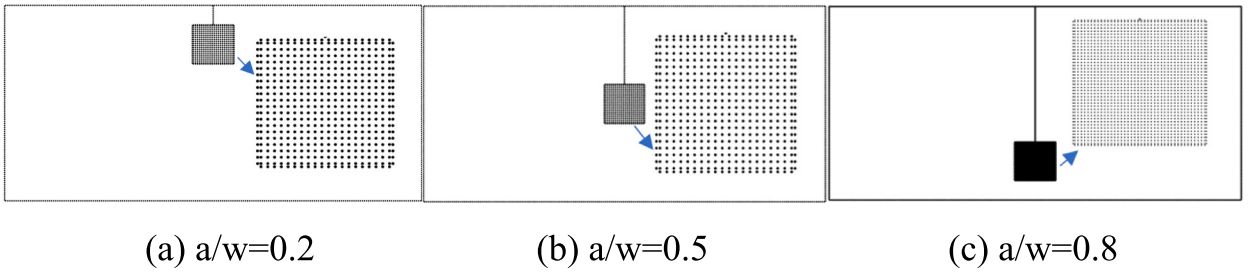


**Fig. 23.** The discretization of a tensile plate with a crack.

in Algorithm 1 is implemented. In this example, the critical bond stretches $s_0 = 0.02$.

As the load increases, the crack propagates. The crack propagation processes at steps 15, 21, and 28, along with their corresponding displacement contours, are depicted in Fig. 26. It can be observed that the PD domain focuses solely on the crack tip, while the micro-cracks propagate within the PD domain. The geometry remains unchanged, only adjusting in response to the crack's movement. As the PD domain moves, the length of the macro crack increases in the macro BEM domain.

### 3.2.3. *Crack propagation in a shear plate*

In this example, a plate with an edge crack is fixed at half of both the top and bottom edges, while a distributed deformation is subjected to the other half of the top edge as shown in Fig. 27. Thus, a shear plate with a 5 m edge crack is studied by the present multi-scale method. The initial deformation is set at 0.08 m, with a deformation step size of 0.02 m. The Young's modulus of the plate is $1 \times 10^4$ Pa, $\nu = 1/3$. An initial macro-BEM model consists of 760 boundary elements, and a fixed PD model includes 20 material points on each side with a total of 400 material points employed at the crack tip. The adaptive dynamic relaxation with a time step of 1.0 s and a total of 500 steps is applied. The PD domain moves 0.5 m for each geometry iteration, and 10 boundary elements are placed along each edge of the extended macro crack. The final convergence is achieved when $\Psi = 1 \times 10^{-2}$ m. The adaptive relaxation parameter outlined in Algorithm 1 is employed, with a critical bond stretch $s_0 = 0.02$.

As deformation increases, the crack propagates. The crack propagation processes at steps 14, 21 and 24, along with the corresponding displacement contours are depicted in Fig. 28. It is evident that, as the shear load increases, the straight crack alerts its direction. The detailed micro crack propagation path is precisely tracked in the PD domain and subsequently transformed into macro crack in the BEM domain.

### 3.2.4. *A rectangular plate with one hole and an edge crack*

A rectangular plate featuring a single hole with a diameter of 10 mm and a 6 mm long edge crack is examined. As illustrated in Fig. 29, a tension load is applied to the right side of plate while the left side is fixed. Young's modulus is 72 GPa, Poisson's ratio is 1/3, fracture toughness is 3288.76 N/mm$^{1.5}$. The BEM model initially contains 904 elements, with 50 elements surrounding both the crack and the hole. Additionally, a fixed PD model with 20 material points on each side and a total of 400 points is employed at the crack tip. The adaptive dynamic relaxation is implemented with a time step of 1.0 s over a total of 1000 steps. The PD domain moves 0.5 m for each geometry iteration, and 10 boundary elements are positioned along each edge of the growing macro crack. The final convergence criterion is set at $\Psi = 1 \times 10^{-2}$ m. The adaptive relaxation parameter in Algorithm 1 is employed. For this example, the critical bond stretches $s_0 = 0.02$. An initial load of 115 MPa is subjected to the right side of the plate, with an increment of 1 MPa at each subsequent step.

The crack propagation processes at steps 31, 50, and 60, along with the corresponding displacement contours, are depicted in Fig. 30. Each contour of damage is accompanied by an enlarged view in the PD domain. Fig. 31 shows a comparison of the crack propagation path result of using the adaptive PD-BEM with results from experimental tests, the extended finite element method

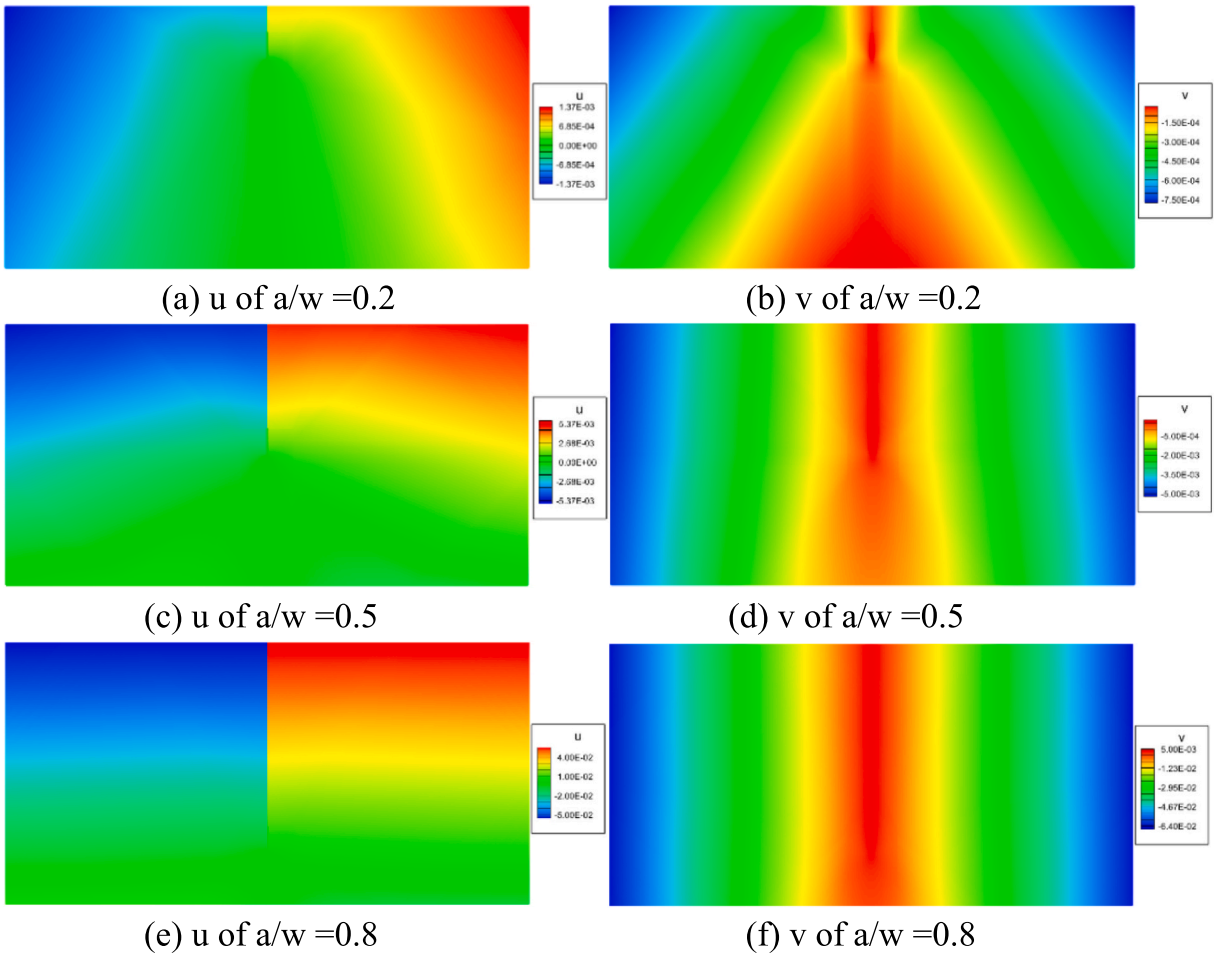


**Fig. 24.** The displacement contours of a tensile plate with a crack.

**Table 3**
Relative errors for different values of $a/w$.

| $a$ | PD-BEM | BEM | Exact results | Error (PD-BEM) (%) | Error(BEM) (%) | Steps | Time (s) |
|---|---|---|---|---|---|---|---|
| 2 | $7.39 \times 10^{-4}$ | $7.21 \times 10^{-4}$ | $7.20 \times 10^{-4}$ | 2.53 | 0.20 | 47 | 22.10 |
| 5 | $4.93 \times 10^{-3}$ | $4.81 \times 10^{-3}$ | $4.92 \times 10^{-3}$ | 0.13 | 2.44 | 39 | 22.28 |
| 8 | $5.26 \times 10^{-2}$ | $5.08 \times 10^{-2}$ | $6.41 \times 10^{-2}$ | 21.79 | 26.00 | 36 | 27.78 |

**Table 4**
Relative errors for $a/w = 0.5$.

| Case | Numbers of BE and MP | PD-BEM ($\times 10^{-3}$) | Error (%) | Convergence factor | Steps | Time (s) |
|---|---|---|---|---|---|---|
| 1 | 760 and 400 | 4.9299 | 0.13 | 0.1 | 39 | 22.28 |
| 2 | 800 and 1200 | 4.9329 | 0.19 | 0.09 | 44 | 53.78 |
| 3 | 800 and 300 | 4.9427 | 0.39 | 0.1 | 39 | 28.22 |

**Table 5**
Relative errors for $a/w = 0.8$.

| Case | Numbers of BE and MP | PD-BEM | Error (%) | Convergence factor | Steps | Time (s) |
|---|---|---|---|---|---|---|
| 1 | 820 and 400 | $5.26 \times 10^{-4}$ | 21.79 | 0.1 | 44 | 27.78 |
| 2 | 1840 and 400 | $5.99 \times 10^{-3}$ | 7.00 | 0.08 | 44 | 229.91 |
| 3 | 3680 and 1600 | $6.16 \times 10^{-2}$ | 4.03 | 0.06 | 59 | 862.38 |

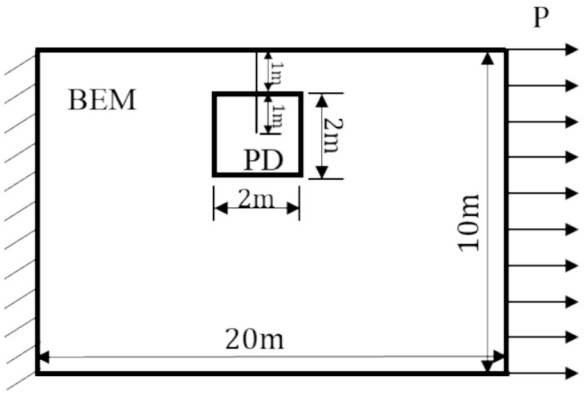


**Fig. 25.** The schematical of a tensile plate with an edge crack.

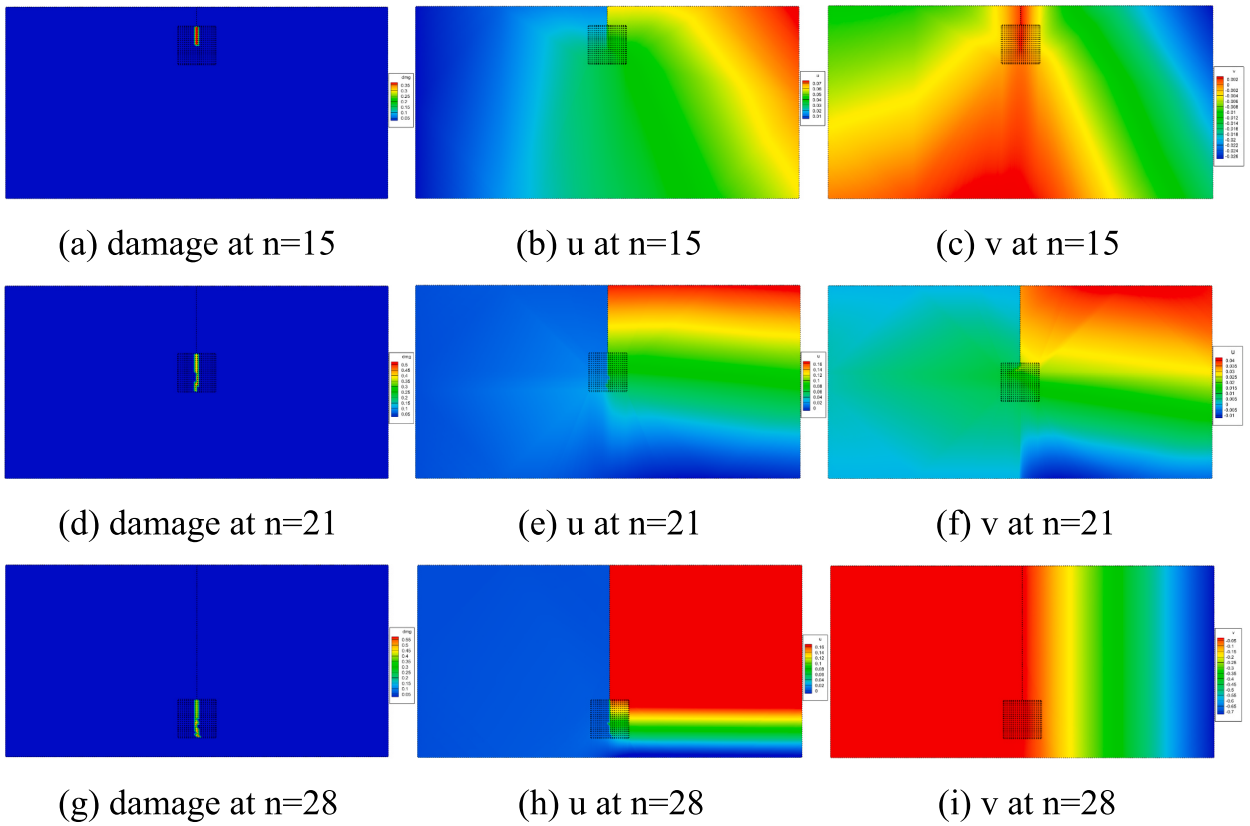


**Fig. 26.** Crack propagation with different time steps for a tensile plate.

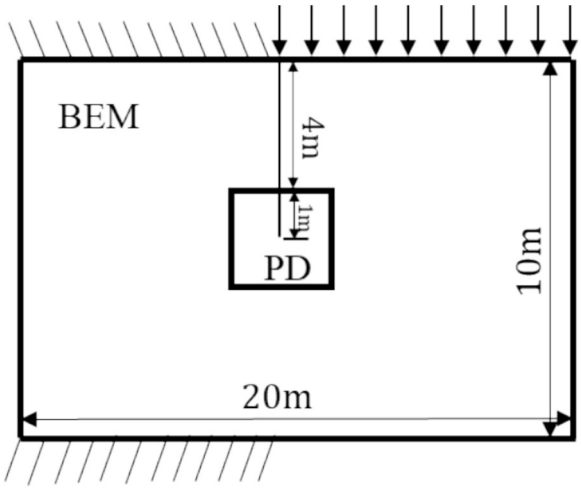


**Fig. 27.** The schematic of a shear plate with an edged crack.

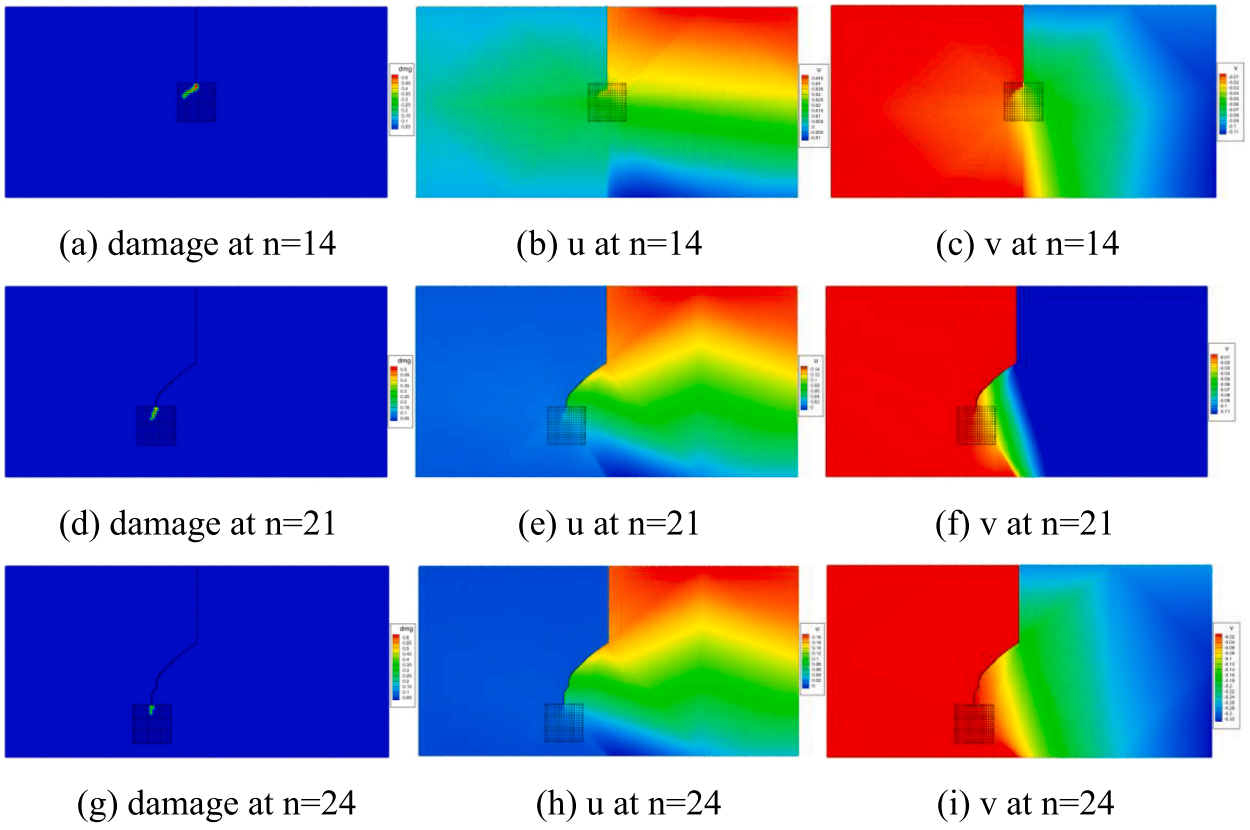


**Fig. 28.** Crack propagation with different time steps for a shear plate.

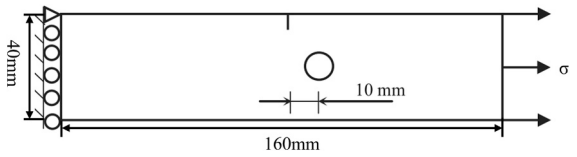


**Fig. 29.** The schematic of a plate with one hole and an edge crack.

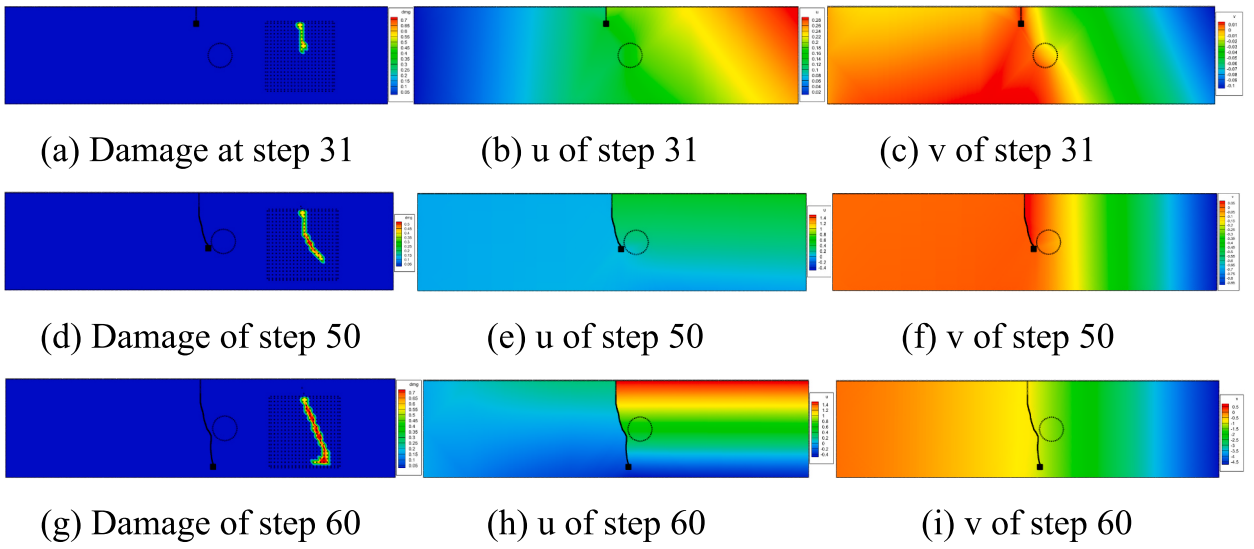


**Fig. 30.** Crack propagation with different time steps for a plate with a hole and an edge crack.

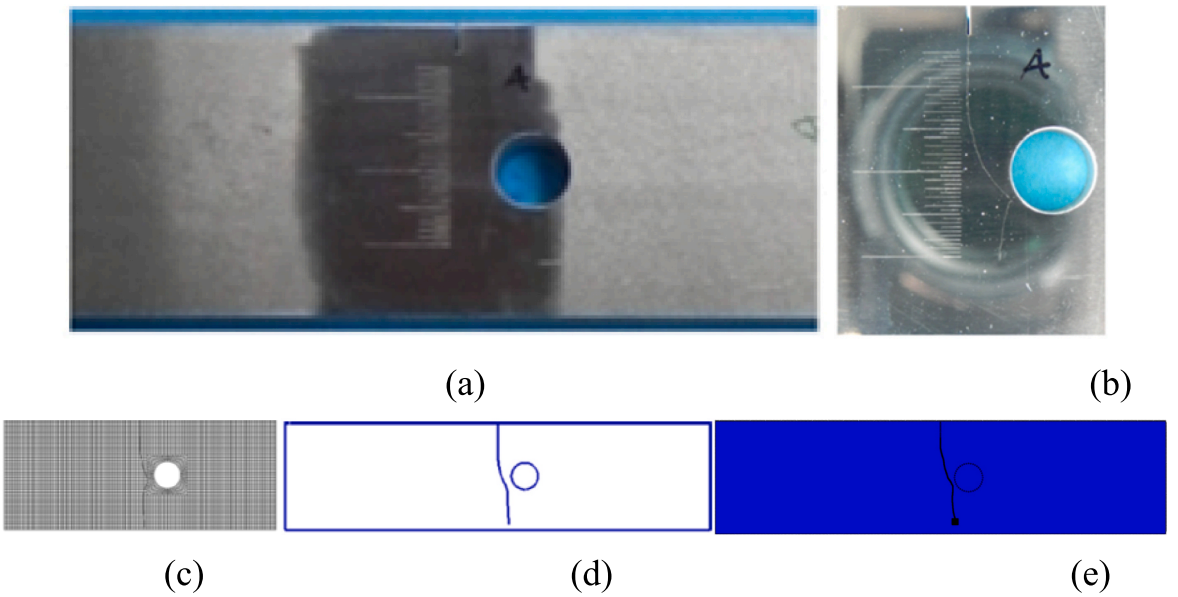


**Fig. 31.** Crack propagation path of the cracked plate with one hole: (a) test sample [42]; (b) test result [42]; (c) XFEM result [42]; (d)FMM BEM result [34]; (e) Present result.

(XFEM) reported in Ref. [37], and the FMM-BEM results in [34]. There is very good agreement among the results from the adaptive PD-BEM, the experimental, XFEM, and FMM-BEM.

## 4. Conclusions

In this paper, a multiscale crack propagation modeling approach based on the adaptive coupling of PD and BEM has been developed. This innovative algorithm can automatically and accurately predict the crack propagation path and direction without relying on predefined crack trajectories. The method takes advantage of PD in accurately tracking the propagation direction of microscale cracks and the transitions during multiscale crack extension. Simultaneously, it preserves the advantages of the BEM in precisely simulating the mechanical responses of macroscopic cracks. Thus, improving the overall performance of the coupled approach. The adaptive coupling iteration scheme enables parallel accelerations of both algorithms, leading to improved computational efficiency. The accuracy and efficiency of the approach are verified through a series of case studies, demonstrating its applicability and reliability. This study contributes to the field of PD research by providing a robust computational tool that can enhance our understanding of crack propagation and improve the predictive capabilities of material failure analysis. This approach has the potential to be applied to the crack propagation analysis of actual structural components.

## CRediT authorship contribution statement

**Yang Yang:** Writing – review & editing, Writing – original draft, Supervision, Methodology, Funding acquisition. **Xun Wei:** Validation, Software. **Yijun Liu:** Writing – review & editing, Conceptualization.

## Declaration of competing interest

The authors declare that they have no known competing financial interests or personal relationships that could have appeared to influence the work reported in this paper.

## Acknowledgments

The authors would like to thank the financial support from National Natural Science Foundation of China (Project Nos. 12272160 and 12372198) and the Shenzhen National Science Foundation (Project No. 20231129213819001).

## Data availability

Data will be made available on request.

## References

[1] Silling SA. Reformulation of elasticity theory for discontinuities and long-range forces. J. Mech. Phys. Solids 2000;48(1):175–209.
[2] Karpenko O, Oterkus S, Oterkus E. Influence of different types of small-size defects on propagation of macro-cracks in brittle materials. J Peridyn Nonlocal Model 2020;2:289–316.
[3] Chen YJ, Yang Y, Liu YJ. Fatigue crack growth analysis of hydrogel by using peridynamics. Int. J. Fract. 2023;244:113–23.
[4] Chen YJ, Yang Y, Liu YJ. Large deformation and crack propagation analyses of hydrogel by peridynamics. Engng Fract Mech 2023;109261.
[5] Wang J, Yu Y, Mu Z, et al. Peridynamic meso-scale modeling for degradation in transverse mechanical properties of composites with micro-void defects. Acta Mech. Solida Sin. 2022;35:813–23.
[6] Ozdemir M, Imachi M, Tanaka S, et al. A comprehensive investigation on macro-micro crack interactions in functionally graded materials using ordinary-state based peridynamics. Compos. Struct. 2022;287:115299.
[7] Hu YL, Yu Y, Madenci E. Peridynamic modeling of composite laminates with material coupling and transverse shear deformation. Compos. Struct. 2020;253:112760.
[8] Shen G, Xia Y, Li W, et al. Modeling of peridynamic beams and shells with transverse shear effect via interpolation method. Comput Method Appl M 2021;378:113716.
[9] Yang Z, Oterkus E, Oterkus S. A novel peridynamic mindlin plate formulation without limitation on material constants. J Peridyn Nonlocal Model 2021;3:287–306.
[10] Yang Z, Oterkus E, Oterkus S. Peridynamic higher-order beam formulation. J Peridyn Nonlocal Model 2021;3:67–83.
[11] Yang Z, Oterkus E, Oterkus S. Peridynamic formulation for higher-order plate theory. J Peridyn Nonlocal Model 2021;3:185–210.
[12] Zhang Q, Li S, Zhang AM, et al. A peridynamic Reissner-mindlin shell theory. Int J Numer Meth Engng 2021;122:122–47.
[13] Yang Y, Chen YJ, Liu YJ. Fracture analysis of hyperelastic membrane using bond-associated non-ordinary state-based peridynamics. Engng Fract Mech 2024;303:110131.
[14] Zhang H, Liu Z, Li C, et al. A stabilized peridynamic correspondence material model for axisymmetric ablation and fracture problems. Comput. Struct. 2024;301:107467.
[15] Li C, Zhang H, Pan C, et al. Implicit stabilized non-ordinary state-based peridynamics for finite deformation and fracture analysis of nearly incompressible materials. Comput Methods Appl Mech Engng 2025;438:117879.
[16] Shojaei A, Hermann A, Cyron CJ, et al. A hybrid meshfree discretization to improve the numerical performance of peridynamic models. Comput Methods Appl Mech Engng 2022;391:114544.
[17] Shojaei A, Hermann A, Seleson P, et al. Peridynamic elastic waves in two-dimensional unbounded domains: construction of nonlocal dirichlet-type absorbing boundary conditions. Comput Methods Appl Mech Engng 2023;407:115948.
[18] Zhong J, Han F, Zhang L. Accelerated peridynamic computation on GPU for quasi-static fracture simulations. J Peridynam Nonlocal Model 2023:1–24.
[19] Yang Y, Su ZX, A state based peridynamic algorithm based GPU parallelism, Chinese Journal of Computational Mechanics. 2024, in press.
[20] Chen YJ, Yang Y, Liu YJ. A neural network peridynamic method for modeling rubber-like materials. Int. J. Mech. Sci. 2024;273:109234.

[21] Yang Y, Chen Y, Liu YJ. A novel neural-network non-ordinary state-based peridynamic method for large deformation and fracture analysis of hyperelastic membrane. Comput Method Appl M 2024;431:117239.
[22] Liu W, Hong JW. A coupling approach of discretized peridynamics with finite element method. Comput Method Appl M 2012;245:163–75.
[23] Bie Y, Cui X, Li Z. A coupling approach of state-based peridynamics with node-based smoothed finite element method. Comput Method Appl M 2018;331:675–700.
[24] Liu S, Fang G, Fu M, Yan X, Meng S, Liang J. A coupling model of element-based peridynamics and finite element method for elastic-plastic deformation and fracture analysis. Int. J. Mech. Sci. 2022;220:107170.
[25] Han F, Lubineau G, Azdoud Y, Askari A. A morphing approach to couple state-based peridynamics with classical continuum mechanics. Comput Method Appl M 2016;301:336–58.
[26] Zaccariotto M, Mudric T, Tomasi D, Shojaei A, Galvanetto U. Coupling of FEM meshes with peridynamic grids. Comput Method Appl M 2018;330:471–97.
[27] Ni T, Zaccariotto M, Zhu QZ, Galvanetto U. Static solution of crack propagation problems in peridynamics. Comput Method Appl M 2019;346:126–51.
[28] Tong Y, Shen WQ, Shao JF. An adaptive coupling method of state-based peridynamics theory and finite element method for modeling progressive failure process in cohesive materials. Comput Method Appl M 2020;370:113248.
[29] Mossaiby F, Sheikhbahaei P, Shojaei A. Multi-adaptive coupling of finite element meshes with peridynamic grids: robust implementation and potential applications. Engng Comput 2022:1–22.
[30] Liu Q, Xin X, Ma J, Adaptive coupling peridynamic least-square minimization with finite element method for fracture analysis, 2022 arXiv preprint arXiv: 2206.09494.
[31] Alebrahim R, Marfia S. A fast adaptive PD-FEM coupling model for predicting cohesive crack growth. Comput Method Appl M 2023;116034.
[32] Liu YJ. Fast multipole boundary element method: theory and applications in engineering. Cambridge: Cambridge University Press; 2009.
[33] Yang Y, Liu YJ. A new boundary element method for modeling wave propagation in functionally graded materials. Eur J Mech A-Solid 2020;80:103987.
[34] Liu YJ, Li YX, Xie W. Modeling of multiple crack propagation in 2-D elastic solids by the fast multipole boundary element method. Engng Fract Mech 2017;172:1–16.
[35] Liang X, Wang L. The Boundary element method for Ordinary state-based peridynamics. CMES-Comp Model Eng 2024;139(3).
[36] Liang X, Wang L, Xu J, Wang J. The boundary element method of peridynamics. Int J Numer Meth Engng 2021;122(20):5558–93.
[37] Yang Y, Liu YJ. Modeling of cracks in two-dimensional elastic bodies by coupling the boundary element method with peridynamics. Int. J. Solids Struct. 2021;217–218:74–89.
[38] Yang Y, Liu YJ. Analysis of dynamic crack propagation in two-dimensional elastic bodies by coupling the boundary element method and the bond-based peridynamics. Comput Method Appl M 2022;399:115339.
[39] Madenci E, Oterkus E. Peridynamic theory and its applications. New York: Springer; 2014.
[40] Kilic B, Madenci E. An adaptive dynamic relaxation method for quasi-static simulations using the peridynamic theory. Theor. Appl. Fract. Mech. 2010;53(3):194–204.
[41] Lin CC, Lawton EC, Caliendo JA, et al. An iterative finite element-boundary element algorithm. Comput. Struct. 1996;59(5):899–909.
[42] Varfolomeev I, Burdack M, Moroz S, Siegele D, Kadau K. Fatigue crack growth rates and paths in two planar specimens under mixed mode loading. Int. J. Fatigue 2014;58:12–9.